

### 3. ION BEAM

In order to reach luminosity goals for the eRHIC, several improvements and upgrades have to be made in ion rings. These upgrades are discussed in this chapter.

The required beam emittance values for eRHIC operation with Au or low energy proton beam are below the typical values used presently at the RHIC operation. The electron cooling technique has to be applied to bring transverse emittances down and maintain them at the required level. The cooling can be used also to reach 20cm rms bunch length required for ion bunches in the eRHIC, or even go to shorter bunches. The electron cooling is described in details in section 3.1.

While ion bunch intensity in the eRHIC is at the level of bunch intensities used at the present RHIC operation, the total beam current should be increased considerably, by about factor 6. All this current increase is provided by increasing number of ion bunches circulating in the RHIC rings. Since the present RHIC RF accelerating system is at 360th harmonic of revolution frequency, the maximum number of bunches which can be put into the ion rings is 360. In reality the necessity for an abort gap will decrease the maximum number of bunches, that can be used, to about 335. Still we will talk about 360 bunch mode, assuming 360 bunch pattern by these words.

In order to maximize the eRHIC luminosity this report evaluated consequences and considered required upgrades to reach 360 bunch mode. The number of issues which rise up with increasing the number of bunches are discussed in section 3.2. They include injection upgrade, the evaluation of pressure rise and electron cloud problems, abort system upgrade and an evaluation of heat load in the cold pipe of ion rings.

Beam instabilities are revised in section 3.3.

The proton polarization issues to provide a proton beam with longitudinal polarization direction at the eRHIC interaction point is discussed in section 3.4. The same section considers using polarized beams of other ion species, with  ${}^3\text{He}^{+2}$  as best possible candidate.

## 3.1 Electron Cooling for eRHIC

### 3.1.1 Luminosity and Electron Cooling

The purpose of the luminosity upgrade for eRHIC is to decrease the emittance of the stored ion beams and maintain it at a required level. This will be achieved with a suitable cooling techniques. Present baseline parameters require the following:

1. Decrease of the transverse emittance of Au ions at 100 GeV energy from the 95% normalized emittance of  $15 \pi \mu\text{m}$  to  $6 \pi \mu\text{m}$ . Presently, emittance is increased during storage time from  $15 \pi \mu\text{m}$  to  $40 \pi \mu\text{m}$  due to the IBS.
2. Decrease of the transverse normalized emittance of protons to  $5 \pi \mu\text{m}$  at lower energies 25-50 GeV.
3. Decrease of the longitudinal emittance which provides bunch shortening. The beta-star function at IP requires shortening of the rms bunch length below 25 cm for both protons and Au ions.

An initial study indicates that all three major tasks described above can be achieved with the electron cooler presently under design for the RHIC upgrade project, designated RHIC II [1]-[2].

### 3.1.2 Electron Cooler

The layout of the cooler is shown in Figure 3.1.

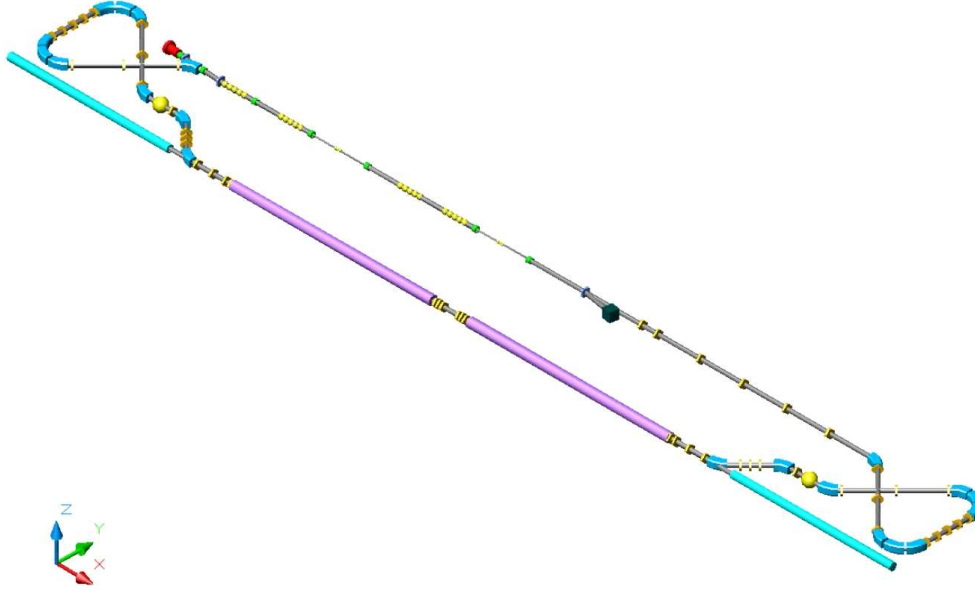


Figure 3.1: Schematic layout of the RHIC electron cooler (system shown for one ring). The photoinjector is shown in red, the superconducting energy-recovery linac is shown in yellow, the solenoid in purple and a section of the RHIC ring is shown in green.

The electron beam will be produced with a cw photoinjector (laser photocathode RF gun), with the cathode of the gun being immersed in a magnetic field to produce a ‘magnetized’ electron beam (an angular momentum dominated beam). Following the initial acceleration in the gun to about 2.5 MeV the beam will be injected into a superconducting energy recovery linac. The beam transport has to preserve the magnetization of the beam in the transport with discontinuous magnetic field. The magnetized electron beam (with its velocity matched to the ion beam) is then introduced into a 1 T cooling solenoid. Since the ion beam is much longer than the electron beam, the phase of the electron beam will be modulated in order to cool the required longitudinal extent of the ion beam. Other modulations (in energy and radial coordinates) may be introduced to shape the ion beam in phase-space. Emerging from the 30 m long cooling solenoid, the electron beam will be separated from the ion beam, rebunched (to match the linac acceptance) and decelerated to recover its energy. The beam will be dumped at about 2.5 MeV.

An R&D on a number of system elements is presently underway [2]: the photoinjector (including its laser and photocathode deposition system), a high-current superconducting cavity for the ERL of the cooler, beam dynamics of the complete system, electron cooling simulation codes and the high-precision superconducting solenoid.

#### Electron gun

An electron beam will be produced with a CW photoinjector (laser photocathode RF gun). It is planned to use CsK<sub>2</sub>Sb (cesium potassium antimonite) cathodes. These cathodes exhibit a very high

quantum efficiency of over 5% for green light. The diode-pumped solid-state laser at a wavelength of 1064nm is planned. The design of the Los-Alamos / Advanced Energy Systems of a 2.5 cell, 700 MHz normal-conducting photoinjector is adopted. The device will be powered by a 1 MW CW klystron and produce about 2.5 MeV beam at over 100 mA. A computer-generated drawing of the photoinjector is shown in Figure 3.2.

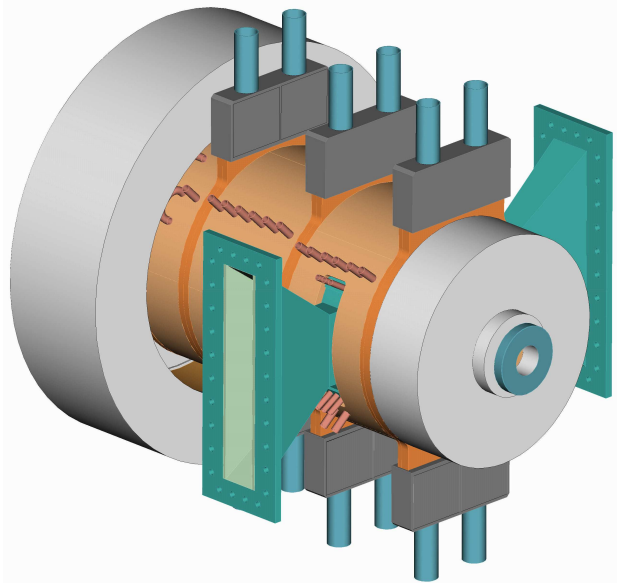


Figure 3.2: The LANL / AES photoinjector which will be used for the electron cooler.

### Energy recovery linac

Following the initial acceleration to about 2.5 MeV the beam will be injected into a 703.75 MHz superconducting Energy Recovery Linac (ERL). Each linac cavity has 5 cells with aperture of 17 cm diameter (see Figure 3.3). The plan is to intercept the Higher-Order Mode (HOM) power by ferrite absorbers located in the beam pipe at room temperature [3]. The cavity opens into a 24 cm beam pipe. This large diameter is chosen in order to conduct the HOM power away from the cavity. For the TE<sub>11</sub> mode, the enlarged pipe (24cm) has a cutoff frequency of 732 MHz, which is below all HOMs. This structure has been simulated by MAFIA computer code [2]. The HOMs with higher frequencies are less important. The simulations show that all the higher order modes couple extremely well to the ferrite, resulting in a beam breakup threshold current of 1.8 ampere.

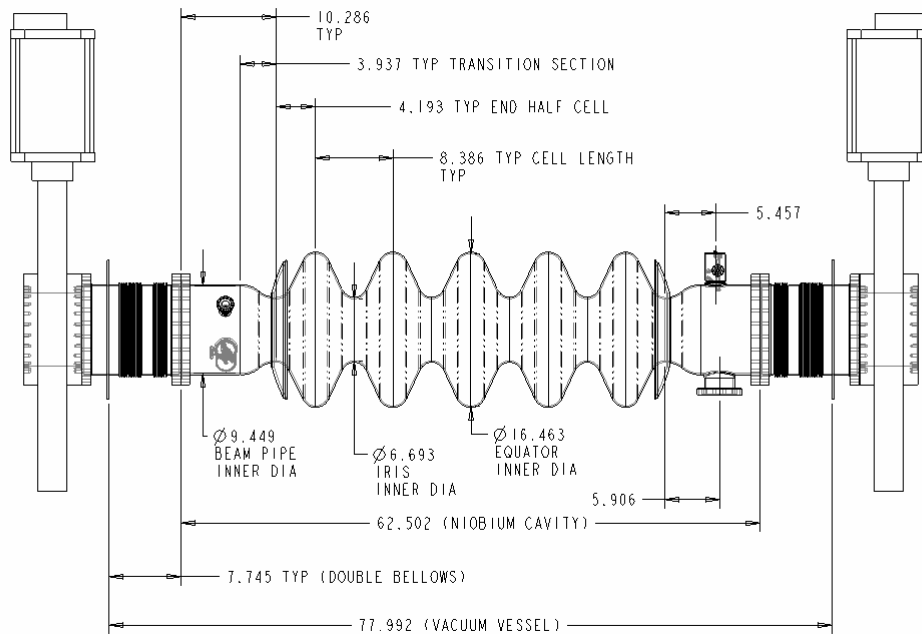


Figure 3.3: A cross section of the superconducting cavity assembly.

### Magnetized beam transport

There are a few straight sections in RHIC where the electron cooler may be introduced. Presently, its placement is considered next to IP4 of RHIC, in the straight section between Q3 and Q4, which can accept about 30 m long solenoids. The electron accelerators will reside outside the RHIC tunnel. The lattice can debunch the beam in order to reduce the space-charge interaction of the electron and ion beams or to reduce the energy spread of the electron beam. The beam transport has to obey certain rules in order to preserve the magnetization of the beam in the transport with a discontinuous magnetic field. Emerging from a long cooling solenoid, an electron beam will be separated from the ion beam, rebunched (to match the linac acceptance) and decelerated to recover its energy. The beam is then dumped at about 2.5 MeV. Merging the low energy and high-energy beams at the entrance of the linac is done using two weak dipoles with a Stabenov solenoid. The linac design assumes the use of 3rd harmonic cavities for additional control of the longitudinal phase space. The two solenoids with opposing fields in the cooling section are proposed to eliminate the coupling in the ion beam. A quadrupole matching section between the solenoids maintains magnetization [4].

### Superconducting solenoid

The superconducting solenoid for electron cooling in RHIC is designed for a 1 T field, with an ample quench margin. The total available space for solenoids is approximately 26 meters. This long solenoid will be manufactured as two shorter sections, 13 m each. The two solenoids will have opposite magnetic field in order to not to introduce horizontal-vertical coupling to the RHIC lattice. A dedicated matching section of 6 quadrupole lenses will flip the direction of the magnetization of the beam between the two solenoids. The solenoid must meet very stringent field quality requirement with a solenoid field-error below  $1 \times 10^{-5}$ . It will also have concentric arrays of ~150mm long vertical and horizontal dipole correctors to compensate for any transverse components. These dipole

correctors will be built using printed circuit coils [5] and will provide corrections of up to 10–3 T with a maximum operating current of 2 A.

### 3.1.3 Cooling Times

Electron cooling times grow with beam energy. As a result, an accurate estimate of cooling times at high-energy becomes extremely important. An order of magnitude estimate, typically sufficient for conventional low-energy coolers, is no longer acceptable. A systematic R&D is presently under way to simulate high-energy electron cooling for RHIC. Presently available analytic formulas for the friction force are different from one another by a significant factor. In addition, the accuracy of their applicability requires detailed examination for the electron cooling parameters relevant for RHIC. A dedicated computer code Vorpel [6] is being developed by Tech-X Company to produce a direct numerical simulation of the friction force and to benchmark available analytic friction-force formulas for RHIC regime of parameters. After detailed benchmarking, reliable friction-force formulas or friction coefficients (directly obtained from simulations) will be used in simulations of the cooling dynamics. Presently, the cooling dynamics is being simulated with the two codes: SimCool [7] and BetaCool [8].

An initial study indicates that cooling in RHIC at full energy for gold ions and some intermediate energy for protons is feasible. The RHIC gold beam evolution is dominated by Intra-Beam Scattering (IBS), which leads to emittance growth and beam loss. Electron cooling is planned during the storage phase of the machine to control IBS and reduce emittances to required values (limited by beam-beam parameters).

Some examples obtained with the BetaCool code (with the parameters of electron cooler given in Refs.[1]-[2]), which show control of the IBS and reduction of beam emittances and bunch length for Au ions at 100 GeV energy, are shown in Figure 3.4 and Figure 3.5 , respectively.

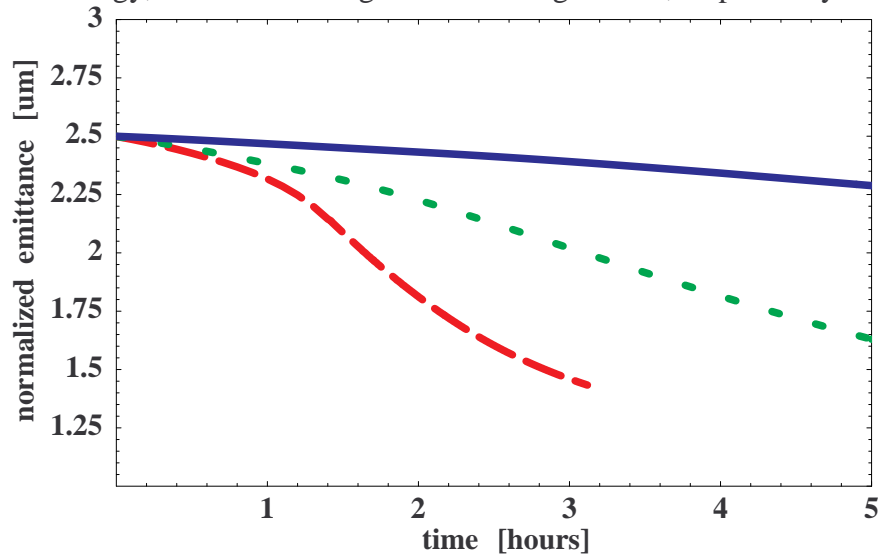


Figure 3.4: BetaCool simulation code: emittance evolution for Au ions (number of ions in a bunch  $N_i=1 \times 10^9$ ) at 100 GeV, with three different electron-cooler currents: 1) number of electrons ( $N_e$ ) in a bunch  $N_e=6 \times 10^{10}$  – blue (solid line), 2)  $N_e=8 \times 10^{10}$  – green (short-dash), 3)  $N_e=12 \times 10^{10}$  – red (long-dash).

Faster cooling times and reduction of beam emittances can be achieved by adjusting beam current in the electron cooler or by employing additional manipulations with the electron beam, which is presently the subject of R&D studies.

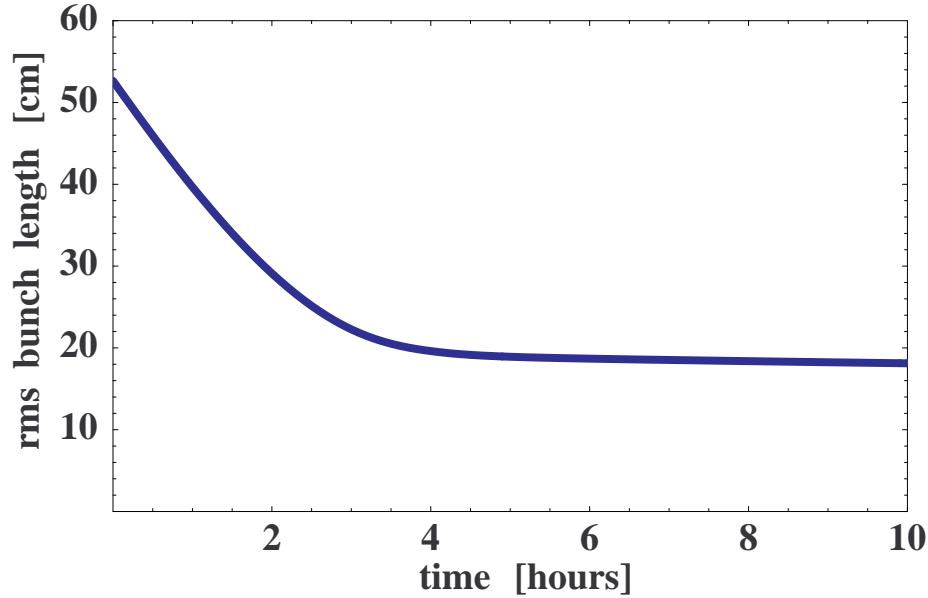


Figure 3.5: BetaCool simulation code: shortening of bunch length for 100 GeV Au ions ( $N_i=1 \times 10^9$ ) with the electron cooler current corresponding to  $N_e=6 \times 10^{10}$  electrons in a bunch.

For protons at high energy in the range of 100-250 GeV, direct electron cooling is not effective. This suggests a staged cooling [9] for high-energy protons, where an initial cooling is first done at low energy close to the injection. In addition, the electron beam area can be varied with time to control reduction of beam emittances to a desired level. At low proton energies in the range 25-50 GeV, cooling becomes more effective and can be used to control transverse beam emittances and an rms bunch length to required values, imposed by an achievable beta-star at the interaction point. Figure 3.6 shows an example for protons at a full energy of 50 GeV, which indicates that beam emittances can be maintained at a required level even when cooling is applied directly at 50 GeV energy.

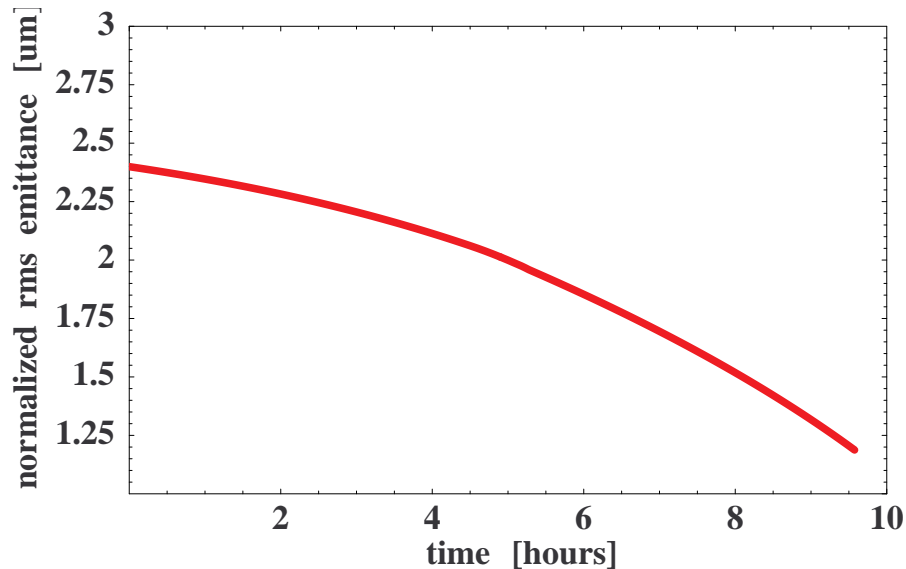


Figure 3.6: BetaCool: rms emittance reduction for 50 GeV protons (number of protons in a bunch  $N_p=1 \times 10^{11}$ ) with the electron cooler current corresponding to  $N_e=6 \times 10^{10}$  electrons in a bunch.

Since electron cooling is effective only at low energy, protons may be first cooled at low energy and then accelerated to a required energy. Figure 3.7 shows emittance reduction for the 27 GeV protons with the number of particles in the electron bunch  $N_e=5 \times 10^{10}$  and  $N_e=1 \times 10^{11}$ , shown with red and green color, respectively. Some reduction of beam emittance with higher electron cooler current maybe found desirable if the beam-beam limit in electron beam is relaxed, as in the case of the linac-ring approach for a collider. Corresponding bunch length compression for low and high current of electron cooler is shown in Figure 3.8 and Figure 3.9, respectively.

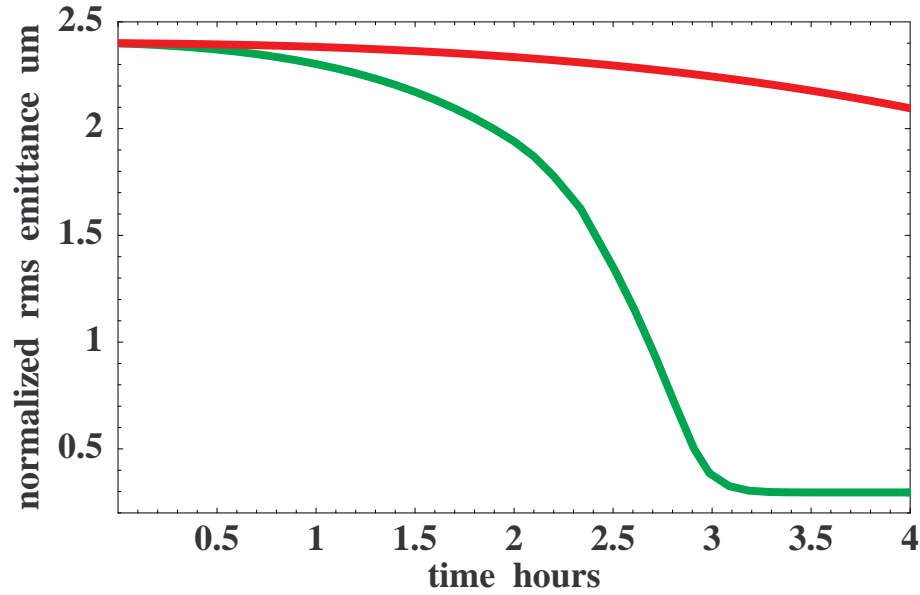


Figure 3.7: BetaCool: rms emittance reduction for 27GeV protons ( $N_p=1 \times 10^{11}$ ) with two currents of electron cooler 1)  $N_e=5 \times 10^{10}$  – red curve, 2)  $N_e=1 \times 10^{11}$  – green curve

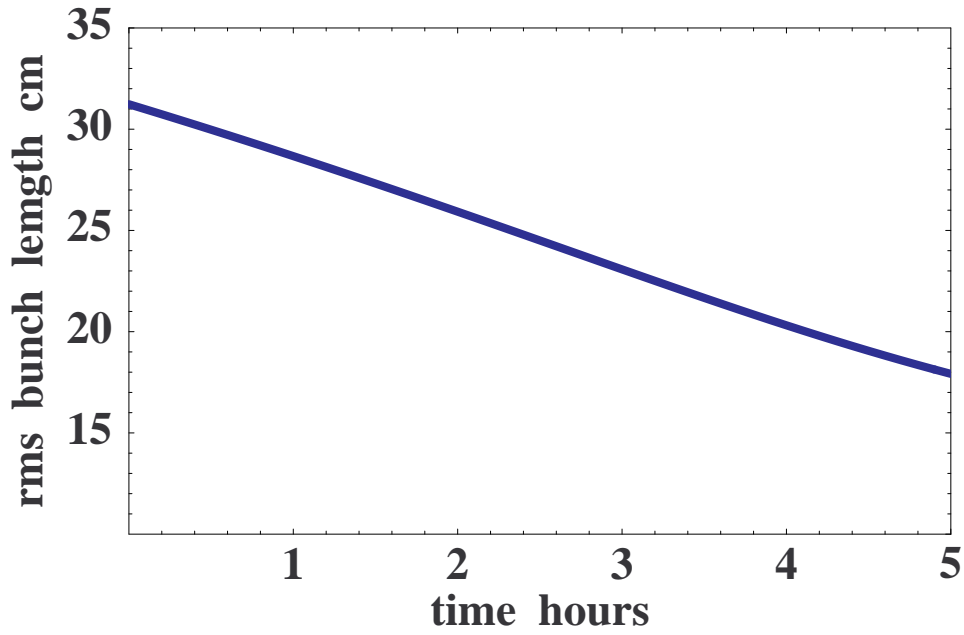


Figure 3.8: BetaCool: rms bunch length compression for 27 GeV protons ( $N_p=1 \times 10^{11}$ ) with  $N_e=5 \times 10^{10}$  electrons in a bunch.

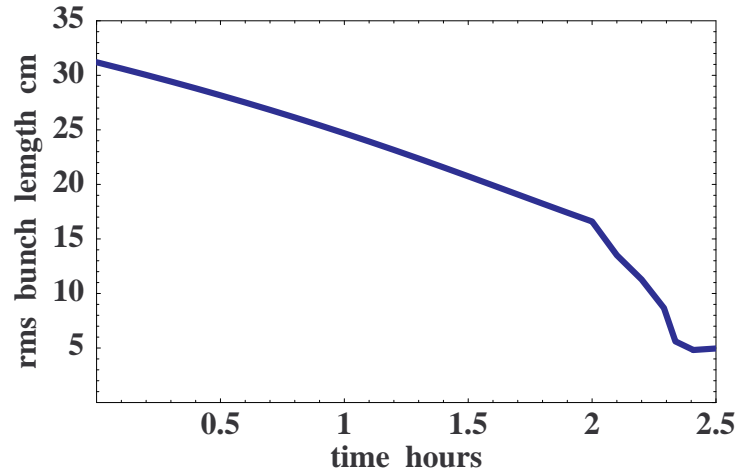


Figure 3.9: BetaCool: rms bunch compression for protons ( $N_p=1 \times 10^{11}$ ) at 27 GeV, with electron cooler current corresponding to  $N_e=1 \times 10^{11}$  in a bunch.

The protons, initially cooled at low energy are accelerated to a full energy of 250 GeV, where only a very weak diffusion due to the IBS occurs. For example, storage at 250 GeV is shown in Figure 3.10 and Figure 3.11 for protons initially cooled to a normalized rms emittance of  $0.8 \mu\text{m}$  ( $4.8 \mu\text{m}$  95% emittance) and  $1.2 \mu\text{m}$  ( $7.2 \mu\text{m}$  95% emittance), respectively. Cooling of protons and Au ion bunches of even higher intensity is discussed in Appendix A.

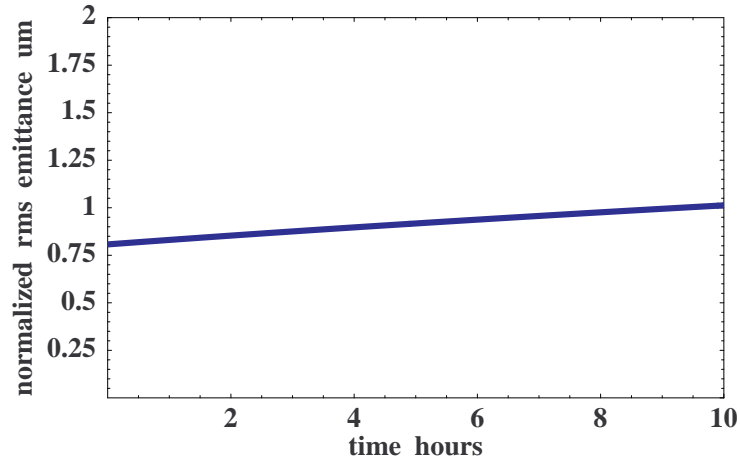


Figure 3.10: BetaCool: Emittance growth at 250 GeV of protons ( $N_p=1 \times 10^{11}$ ) initially cooled to an rms emittance of  $0.8 \mu\text{m}$  at 27 GeV, with the electron cooler current corresponding to  $N_e=1 \times 10^{11}$  in a bunch.

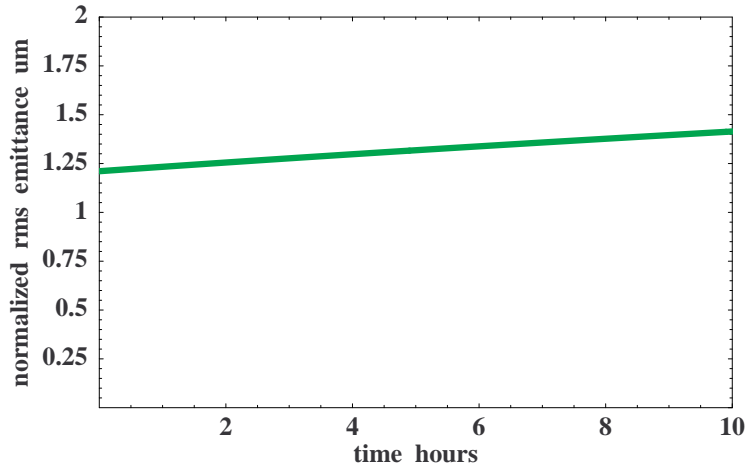


Figure 3.11: BetaCool: Emittance growth at 250 GeV of protons ( $N_p=1 \times 10^{11}$ ) initially cooled to an rms emittance of  $1.2 \mu\text{m}$  at 27 GeV, with the electron cooler current corresponding to  $N_e=1 \times 10^{11}$  in a bunch.

In figures from Figure 3.4 to Figure 3.11, time evolution is shown for the rms beam parameters. However, the process of electron cooling results in a rapid cooling of the core of beam distribution. This feature has a unique application to cooling in a collider: even for a relatively weak cooling of rms beam parameters one can get a significant luminosity gain as a result of cooled beam core. This major feature of electron cooling in a collider is shown in Figure 3.12-Figure 3.15. In this example, the parameters of the electron cooler are chosen such that the rms beam emittances stay approximately constant during the cooling time, as shown in Figure 3.12 for the unnormalized transverse rms emittances.

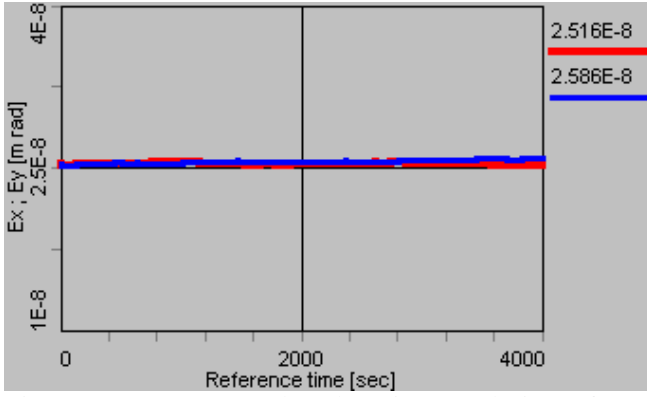


Figure 3.12: BetaCool code: Time evolution of unnormalized rms emittances for Au ions ( $N_i=1 \times 10^9$  in a bunch) at storage energy of 100 GeV for a typical parameters of electron cooler with  $N_e=6 \times 10^{10}$ .

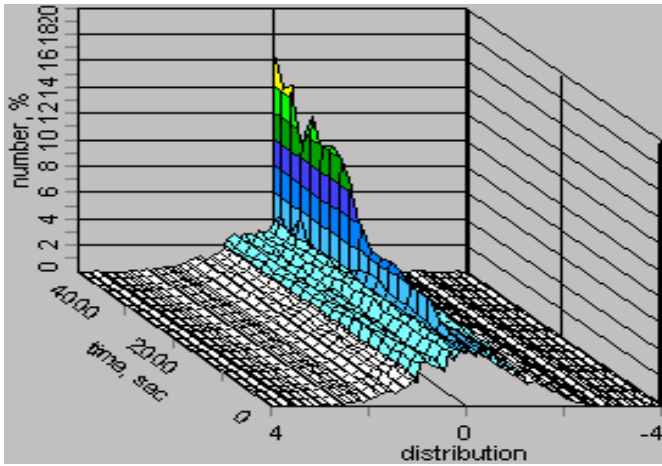


Figure 3.13: BetaCool code: Time evolution of longitudinal beam profile ( $4 \sigma$ ) for the same parameters of electron cooler as in Figure 3.12.

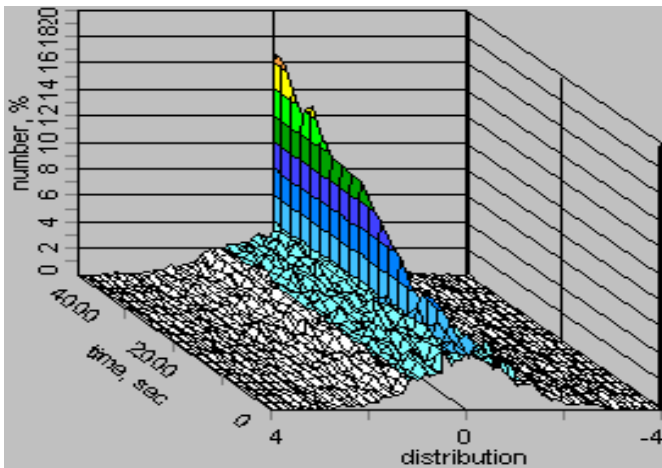


Figure 3.14: BetaCool code: Time evolution of horizontal beam profile ( $4 \sigma$ ) for the same parameters of electron cooler as in Figure 3.12.

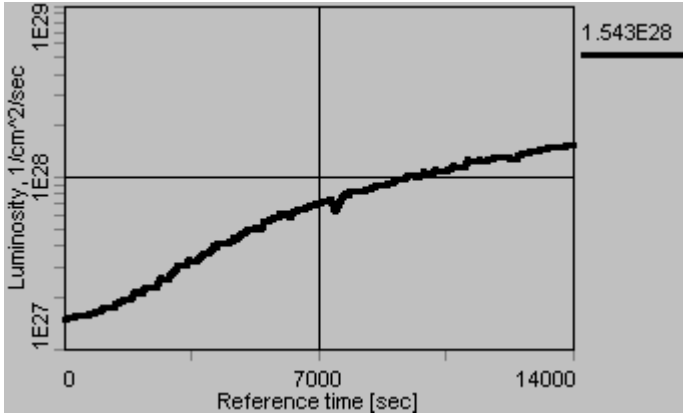


Figure 3.15: BetaCool code: Example of the luminosity increase for Au-Au collisions in RHIC at 100 GeV due to a cooled beam core (Figure 3.14) even for the case when there is no rapid cooling of the rms beam parameters, as shown in Figure 3.12.

A detailed benchmarking of simulation codes is presently in progress.

## 3.2 Towards 360 Bunches in RHIC

To achieve a high luminosity in eRHIC, the bunch number in the hadron ring of RHIC needs to be maximized while the bunch spacing in the hadron and electron rings needs to be the same. With larger bunch numbers, and consequently larger beam currents, a number of effects must be addressed. Among those are

1. Acceleration of high intensity beams
2. Vacuum breakdown with high intensities
3. Increased heat load to the cryogenic system
4. Instabilities, single and multi-bunch
5. Long-range beam-beam interactions
6. Radiation safety concerns with high intensity beams
7. Injection

### 3.2.1 360 Bunches Injection

Currently the maximum number of bunches is 112, limited by the injection kicker rise time and the need for an abort gap. After summarizing the current injection scheme, we discuss 3 options to get to larger bunch numbers in RHIC:

1. Very fast injection kickers
2. Long flattop injection kickers
3. Barrier rf stacking and bunching into the current 28 MHz acceleration system

The first and third option has not been demonstrated at another accelerator with beam parameters comparable to those required at RHIC. The second option resembles injection schemes use at HERAp, and foreseen for the LHC.

### The existing injection scheme

Bunches are transferred from the AGS to RHIC one-by-one, and placed into one of the RHIC accelerating buckets of harmonic 360. With this scheme the harmonic numbers of the AGS and RHIC are independent. The injection kickers rise for each bunch, and have an integrated strength to provide a 1.5 mrad kick for the beam of 81 Tm rigidity. The kicker flattop to accommodate a single bunch. In this way, the bunch spacing is limited by the injection kicker rise time. A gap is needed to allow for the abort kicker to rise without kicking beam into the superconducting magnets. Injection kicker rise time and abort gap currently limit the number of bunches to 112, with two empty buckets between filled ones. The main parameters of the existing injection system are listed in Table 3.1.

Table 3.1: Main parameters for the current injection system for hadron beams

Parameter	Symbol	Unit	Value
Beam rigidity	$B\rho$	Tm	81
Rf frequency	$f_{\text{rf}}$	MHz	28
Harmonic number	$h$	...	360
Bucket length	$l_{\text{bucket}}$	ns	36
Total bunch length	$l_{\text{bunch}}$	ns	15
Injection kicker rise time	$t_{\text{rise}}$	ns	95
Revolution time	$T_{\text{rev}}$	$\mu\text{s}$	12.8
Abort gap	$t_{\text{abort}}$	$\mu\text{s}$	0.85

### Very fast injection kickers

If the injection kicker rise time could be shortened, more bunches could be injected with the existing scheme. With the existing bucket spacing, bunch length, and abort gap (see Table 3.1), the injection kicker rise time would need to be 57 ns or less if every other bucket is filled (allowing for a total of 168 bunches), and 20 ns or less if every bucket is filled (allowing for a total of 336 bunches).

Reducing the injection kicker rise time in RHIC is limited by several conceptual and technological constraints. The present system is well understood and can serve as basis for scaling. The four injection kickers are in a warm space of 5.4 m length, between the flanges to the Q90 and D90 magnets. The physical magnet length is 1.12 m, and the effective ferrite length 80 cm. The magnet is designed as an all-ferrite transmission line with 40  $\Omega$  characteristic impedance. The propagation velocity was measured to be 3.3 cm/ns (one ninth the speed of light). The thyatron pulser delivers a pulse with a 33 ns rise time. In order to avoid voltage breakdown, the kicker is presently operated with a mismatched 25  $\Omega$  termination, resulting in an effective rise time of 95 ns.

The design concept for the present kicker system can accommodate the rise time requirement for a 180 bunch pattern. This can be achieved by operating the kicker fully matched, leading to a pulse transit time of 24 ns which together with the pulser rise time of 33 ns leads to the required 57 ns. Necessary changes must address the voltage limitation in the kicker:

- Currently only 60% of the available warm space is filled with ferrite, and a fifth magnet may be fitted in. The additional magnet can serve to sufficiently reduce the operating voltage while retaining the present kicker constructions. Alternatively, the transit time in a shortened magnet leads to gains of about 5 ns in rise time.

- Another solution would be to adopt conventional plate kickers designed for  $25\ \Omega$  to match the present Blumlein pulser. However, the transit time would be increased to an unacceptable 38ns. By accepting the reflections at the kicker input, which the present system tolerates, one can design the plate kicker for  $40\ \Omega$ , or even  $50\ \Omega$ , and operate it with matched termination.

Whereas a solution for the 180 bunch pattern is plausible within presently available technology, the requirements for a single bunch injection with 20 ns rise time in the 360 pattern are extreme. An advanced R&D program at the Lawrence Livermore National Laboratory (LLNL) has the goal of achieving 10 ns rise times in pulsers using solid state Metal Oxide Semiconductor Field Effect Transistors (MOSFET) and Insulated Gate Bipolar Transistors (IGBT). Assuming that 10 ns can be obtained at the current/voltage level required, only 10 ns remains for the transit time in the kicker. Thus, the effective kicker length is limited to 33 cm provided by 10 units. Although in principle possible, this solution would require a completely new injection system, kicker magnets and pulsers, as well as dramatic technology breakthroughs and corresponding R&D efforts.

### Long flattop injection kickers

With a long flattop of the injection kickers, a whole AGS fill could be transferred at once. This would require a new rf system in the AGS and a completely new injection system. With about 6 such transfers, RHIC would be filled. For this the bucket length in the AGS and RHIC must be the same. That could be achieved by having a 28 MHz system in the AGS. The circumference of RHIC is  $19/4$  of the AGS circumference. If the RHIC harmonic number remains unchained, the AGS extraction would need to be performed at a non-integer harmonic. Furthermore, about 20 times more intensity would need to be accelerated in AGS than with the current scheme, while preserving the transverse and longitudinal emittances. With 20 times more booster cycles needed to fill the AGS, some part of the beam would stay significantly longer at AGS injection, subjecting it to space charge and possibly intra-beam scattering effects. The large number of Booster cycles needed to fill the AGS may also raise issue with the local electricity utility. In this scheme, however, the rise time is a less critical issue since a few gaps in the bunch train would have only a small effect on the luminosity.

### Barrier rf stacking

By employing a barrier bucket system in RHIC it is, in principle, possible to inject a large number of bunches without constraints from the injection kicker rise time. A barrier bucket system creates only a few rf wave forms per turn. In this way, beam can be held in a large part of the circumference, and new bunches injected in buckets that are then merged into the long bunch (see Figure 3.16). After injection of all bunches, the beam can be bunched with the 28 MHz acceleration system, and accelerated to the store energy.

First consider the rf gymnastics that was used in an AGS experiments. A schematic plot of the net voltage per turn for injection above transition is shown below. Note that the time scale is very different from what would actually occur so as to make details clear.

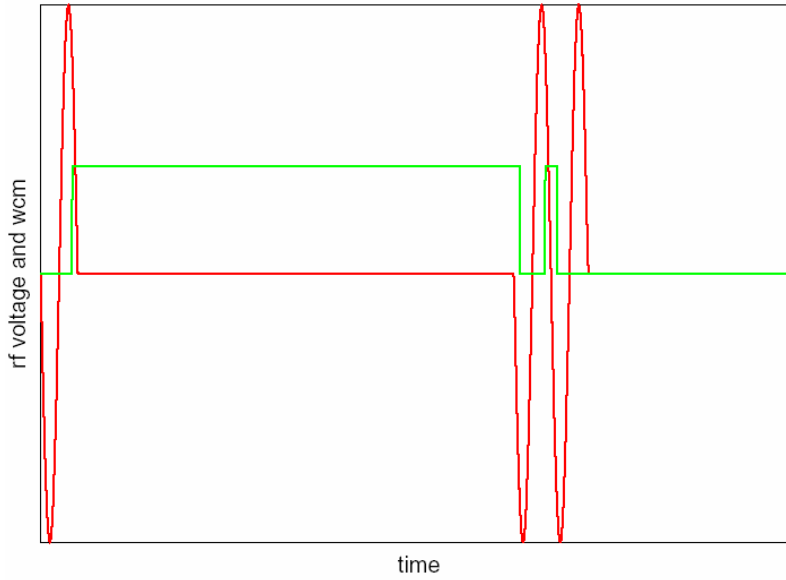


Figure 3.16: Rf voltage (red) and beam current (green) over one turn.

The rf waveform is shown in red, and wall current monitor signal in green. A bunch has just been injected between the closely spaced barrier waveforms, while beam is held in a large part of the circumference. The next step is to adiabatically lower the barrier between the freshly injected bunch and the long bunch. The voltage waveform confining the right side of the injected bunch would need to be tuned so that the merge conserves emittance. Naively, the relevant time scale for the merge to conserve emittance is the time it takes a particle to perform one oscillation in the long bunch,  $T_{\text{ad}} = T_{\text{rev}}/\Delta f$ . For an rms momentum spread of  $\delta p/p = 0.001$  one finds  $T_{\text{ad}} = 29$  s for  $\gamma = 25.9$ , which is far too long to be practical.

The time required for the merge can be shortened with a technique that does not require a change in the momentum spread of the stored bunch. One way to accomplish this is to shift both the amplitude and the timing of the waveforms that confine the injected bunch as the merge proceeds.

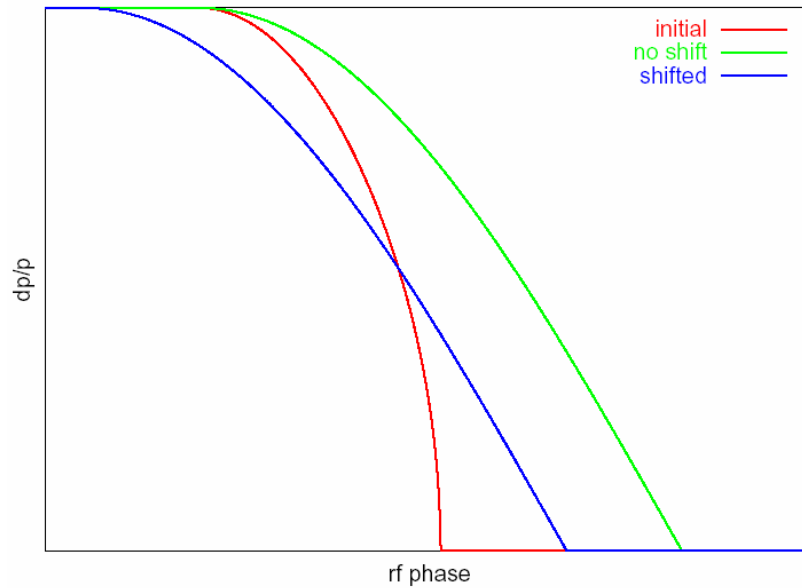


Figure 3.17: Phase space distribution of the long bunch, before and after a merge without and with shifted barrier voltage.

Figure 3.17 shows the longitudinal phase space area before and after a bunch merge. The red curve shows the initial phase space boundary of the stored bunch. If the voltage of the barrier between the stored and injected bunches is simply lowered the green curve results. If the process were completely adiabatic the green curve would have a smaller peak value than shown. However, if the barrier voltage is simultaneously shifted and lowered, the blue curve could be obtained. The areas under the blue and red curves are the same. The adiabatic time in this case is reduced by the ratio of the barrier length to the machine circumference, of order 0.01 in our case. This would allow for bunch transfers every 300 ms.

Another option is a technique described by K.Y. Ng in [10], which employs barrier voltage waveforms that do not change sign in the merging region. The bunch is injected off momentum, and accelerated through the barrier into the stored bunch. This is likely to result in an emittance growth of about 50%.

### Summary

To increase the bunch number in RHIC beyond the current value, a number of problems need to be considered. One of the most severe problems is the injection scheme. We considered very fast injection kickers, long flattop injection kickers, and barrier rf stacking, to fill close to 360 bunches in RHIC. The parameters of all three options are beyond the operating conditions of any existing machine. Thus, significant research and development is needed for either option.

## 3.2.2 Pressure Rise and Electron Cloud

This section reviews presently existing limitations on ion beam intensity due to pressure rise and electron cloud effects. Plans to overcome the limitations in order to increase the number of bunches, ultimately to 360, are considered.

### Injection pressure rise

Pressure rise at the injection has been observed for gold, deuteron, and proton operations in the RHIC. This pressure rise limits operation of 112 bunches with bunch intensity of  $10^9$  gold ions, and  $10^{11}$  for protons [11].

It has been diagnosed that the injection pressure rise is due to the electron multipacting, i.e. electron cloud. The evidences include,

1. Electron detector signals are very closely related with the pressure rise, at onset, saturation, and drooping.
2. Pressure rise and electron signal are very sensitive to the bunch spacing, 112 bunch mode is much worse than 56 bunch mode. Note that the sensitivity to bunch spacing is an important characteristic of the electron cloud.
3. Bunch gap helps.
4. Solenoid field at 5 to 50 Gauss can suppress both pressure rise and electron signal, but not completely.
5. Beam scrubbing has been demonstrated helpful in reducing pressure rise.

On the other hand, the electron cloud observed at the RHIC is different from other machines. For example, the RHIC electron cloud takes place at the bunch spacing of 108 ns or even 216 ns. All other machines have much smaller bunch spacing.

1. The B factories, KEKB and PEP II, have bunch spacing of 4 ns to 8ns.

2. Electron cloud was peaked at 20 ns of bunch spacing at the APS of Argonne.
3. SPS observed electron cloud at 25 ns bunch spacing with the threshold of bunch intensity of 3 to  $4 \times 10^{10}$  protons. At the bunch spacing 130 ns, no electron cloud observed at the bunch intensity of  $2.5 \times 10^{11}$  protons.
4. Tevatron observed electron cloud at 18.9 ns bunch spacing with the bunch intensity of  $4 \times 10^{10}$  protons. The situation is very similar to SPS. The Tevatron Run II plan calls for 132 ns bunch spacing with bunch intensity of  $2.7 \times 10^{11}$  protons.

The RHIC pressure rise and electron cloud have several distinguished characteristics from other machines.

1. It only takes place in warm sections, and the pressure rise distribution in the ring is very un-uniform. When pressure rise at certain location(s) is high enough to close the vacuum valve, many locations have none. The worst locations also may change.
2. Given same chambers, the beam intensity threshold at the Q3 to Q4 straight section, 34 meters long, is only 60% of that at the interaction straight section, which is 17 meters long.
3. No noticeable cryogenic heat load has been observed. Together with the absence of electron cloud induced beam instability and emittance growth, it is believed there is no electron multipacting at the RHIC cold region.
4. RHIC pressure rise decreases at the ramp, and it is non-existent at the store. In SPS, the electron activity was stronger at the store than at the injection [12].

It is suspected that the beam halo scraping at the wall, which generates mostly positive ions, may have helped the secondary electron to survive long bunch gaps, and makes electron multipacting possible. If this is the case, then most RHIC injection pressure rise observations can be explained.

During the 2003 polarized proton run, a beam scrubbing was studied. Total high intensity beam scrubbing time was less than 1 hour. However, beam scrubbing effect was observed not only in the locations with highest pressure rise, but also in others with non-trivial pressure rise. The feasibility of applying the beam scrubbing in RHIC to allow for higher beam intensities has been confirmed.

In Figure 3.18, it is shown that for locations with high pressure rise at about  $5 \times 10^{-6}$  Torr, the pressure rise kept about the same for 3 fills. For locations with medium pressure rise of about  $5 \times 10^{-7}$  Torr, the pressure rise increased. For locations with low pressure rise at less than  $5 \times 10^{-8}$  Torr, the pressure rise of 3rd fill is about 2.5 times higher than the first fill, which is approximately reflecting the beam strength in terms of exciting electron multipacting.

In Figure 3.19, the scrubbing effect at all locations in the ring is displayed against the dose. Note that the dose is defined as the pressure rise times the beam scrubbing duration.

For RHIC operation, the complete elimination of the injection pressure rise is not necessary. Therefore, a limited time of high intensity beam run might be sufficient to allow beam injection with higher intensity.

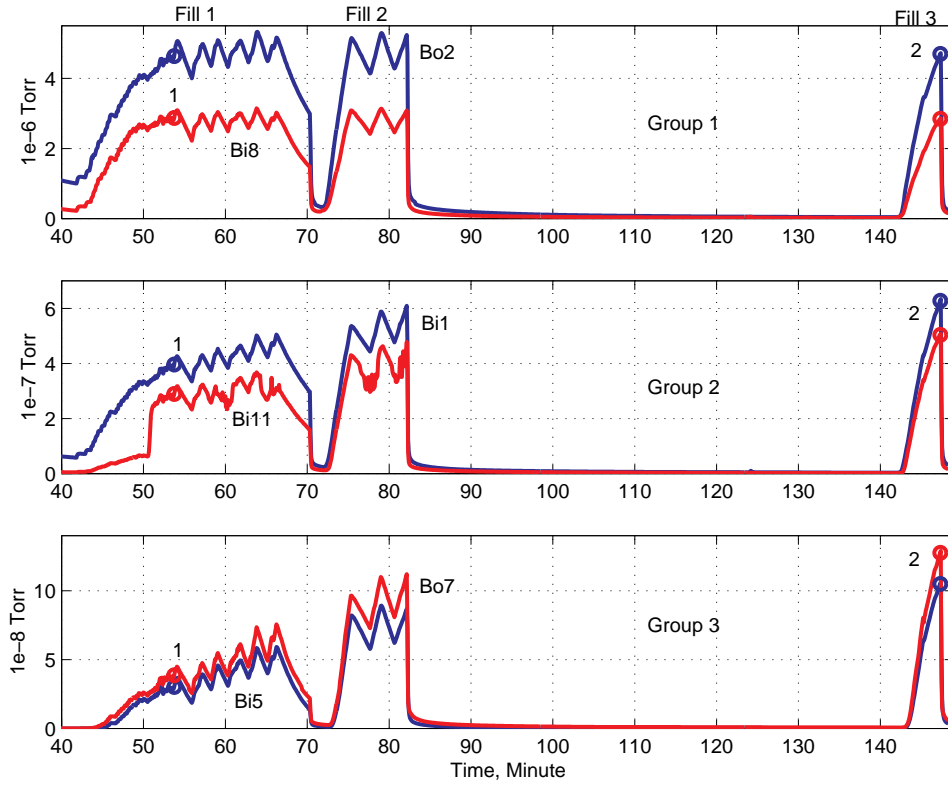


Figure 3.18: Typical pressure rise pattern for three different groups, with the high, medium, and low pressure rises.

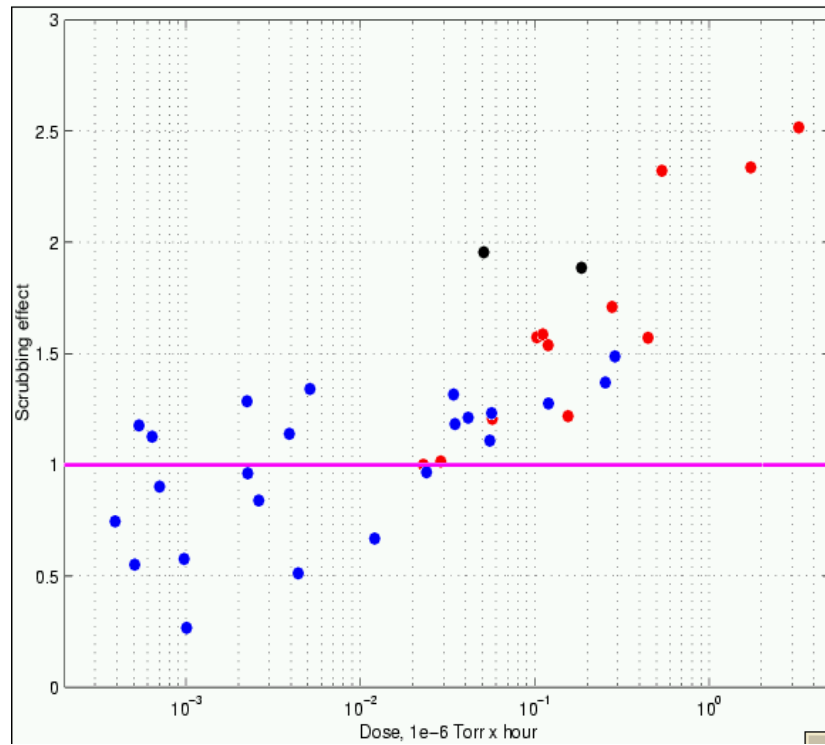


Figure 3.19: Beam scrubbing effect. Unit 1 means no scrubbing effect. Red dots are for the Q3-Q4 single beam straight sections. Black dots are special ones in sections 4 and 10. Blue dots are for interaction regions.

### Transition pressure rise

The beam transition pressure rise for heavy ion operations is another intensity limit for the RHIC. In Figure 3.20, the transition pressure rises in the deuteron-gold (d-Au) run at IR2(BRAHMS), IR10(PHOBOS), and IR12 are shown against the total beam intensity. Intensity unit is charge equivalent to  $1e9$  Au ions.

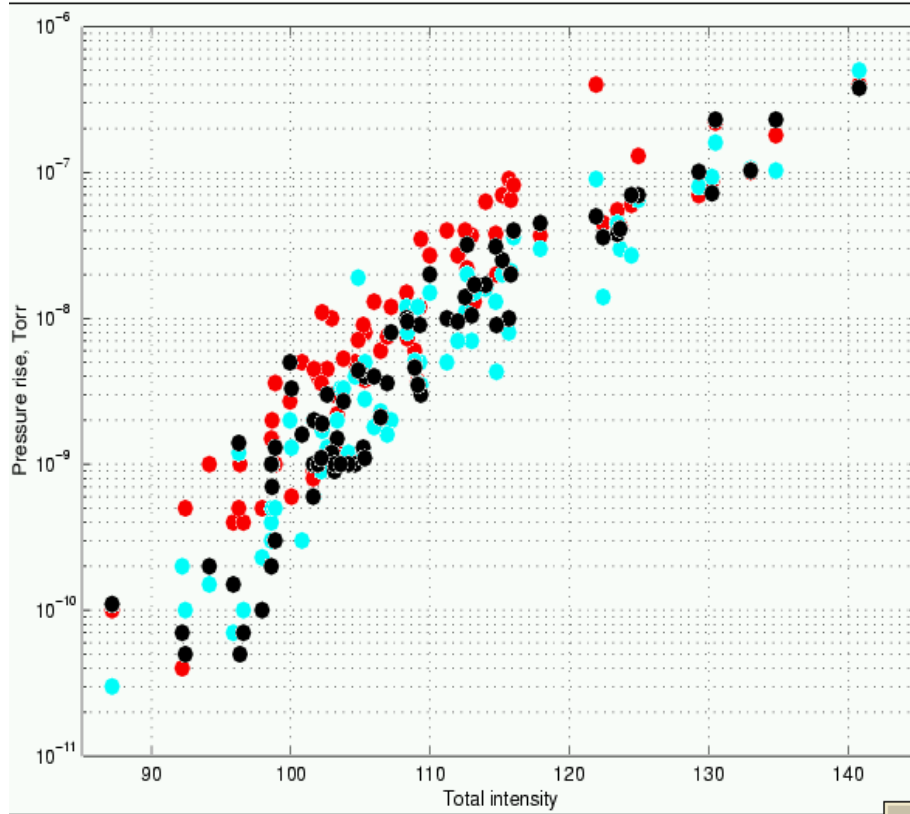


Figure 3.20: Transition pressure rise at IR2 (red), IR10 (cyan), IR12 (black).

The characteristics of this pressure rise are as follows:

1. The pressure rise is quasi-exponentially proportional to the total beam (charge) intensity.
2. For same intensity, no difference between 56 bunch and 112 bunch modes can be identified. The absence of bunch spacing effect indicates that the transition pressure rise is not dominated by the electron cloud. Another evidence is that no electron multipacting signal has been detected at the transition.
3. In Figure 3.20, most high intensity ramps are included, where the beam loss at the transition varies from less than 1% to larger than 10%. The reasonably narrow band in the pressure rise distribution indicates that the beam loss is not a dominant factor.
4. The pressure rise is not related to the ion species. The gold beam intensity was considerably higher than the deuteron in early run. After the deuteron bunch merge in the AGS Booster, the deuteron intensity was much higher than gold beam. No difference can be identified regarding to these different beams. Since the gold ion gas desorption cross section is about 79 times larger than the deuteron ion, this indicates that the gas desorption is not a dominant factor in the transition pressure rise.

It is found that the transition pressure rise is, on the other hand, related to the beam momentum spread:

The beam momentum spread is 0.17% at the injection, it is peaked at 0.3% at the transition, and decreases afterwards. The pressure rise follows this pattern. In proton run, the beam momentum spread decreases in the acceleration, and the pressure rise decreases as well.

The bunch length seems not a dominant factor in the transition pressure rise. At the beam rebucketing, where the bunch was captured in 200 MHz storage cavity, the bunch length reduces to 5 ns, the same as that at the transition (the beam potential at the rebucketing is actually 37% higher than that at the transition due to the smaller transverse size), yet no rebucketing pressure rise observed in the d-Au run.

The total storage cavity voltage was 2.5 MV in d-Au run. At the rebucketing, the beam momentum spread was 0.17%, the same as that at the injection, and much lower than 0.3% at the transition. This may explain the absence of the pressure rise at the rebucketing.

In Run 4, two more common cavities have been commissioned to increase the total rebucketing voltage to 4 MV. The beam momentum spread at the rebucketing becomes larger than 0.19%. The pressure rise was observed at several interaction regions. Much higher storage voltage and the better rebucketing imply higher beam peak current and beam potential. Accordingly, some electron multipacting may have been observed at the rebucketing in Run 4.

The transition pressure rise had caused serious experiment background problem in d-Au run. For same luminosity, 56 bunch mode requires 30% less total intensity than the 112 bunch mode. Switching from 112 bunch mode to 56 bunch, the experiment background was significantly improved. One might expect that the background problem will be relevant again at higher beam intensity, since given 56 bunch mode, the luminosity increases at the square of the bunch intensity, whereas the transition pressure rise is quasi-exponential to that.

Some NEG (non-evaporable-getter) pipes have been installed in the RHIC rings for test. Very rough surface of the activated NEG coating is essential for better pumping. As by-products, the SEY (secondary electron yield) and electron desorption reductions have been measured for the NEG coating, where the rough surface may have contributed. To alleviate the transition pressure rise, ion desorption reduction might be more important. The data on this aspect is, however, less than sufficient. The NEG pipes in RHIC have made possible for the evaluation on ion desorption, and also other issues, such as the activation condition, the saturation effect, the aging, venting effect, possible dust, and impedance problem, etc.

For same purpose, a test stand has been built at the Tandem Van de Graaff. Different activations will be tested, and also the ion desorption on the shallow angle ion beam scraping on stainless steel and NEG surface will be compared.

### Scenario of 360 bunches in RHIC

In the scenario of 360 bunches in the RHIC, not only the injection and transition pressure rises, but also a usual electron cloud may take place for both proton and heavy ion beams. With the bunch spacing of 35 ns, eRHIC is very similar to SPS and LHC in terms of electron multipacting. In Table 3.2, the eRHIC heavy ion and proton parameters are compared with the SPS and LHC, where  $\langle \Delta E \rangle$  is the energy gain per bunch passing.

Table 3.2. Parameters defining electron multipacting for eRHIC, SPS and LHC

Injection/store	eRHIC, Au	eRHIC, p	SPS	LHC
Kinetic energy, $E_k$ , $GeV/u$	8.9/100	24/250	26/450	450/7000
Charge per bunch, $N_{bh}$ , $10^{11}$	0.79	1	1	1
Bunch spacing, $t_{bs}$ , $ns$	35	35	25	25
Chamber radius, $b$ , $cm$	3.45	3.45	2.5	1.74
Beam radius, $a$ , $mm$	3.0/0.93	1.9/0.59	3.2/0.78	1.15/0.293
Energy gain, $\langle \Delta E \rangle$ , $eV$	104/154	198/277	267/450	728/1095

The bunch spacing is one of the most important parameters. In general, larger the bunch spacing, less the secondary electrons survive the bunch gap, and higher SEY is needed for electron multipacting. The 35 ns bunch spacing at the eRHIC is only a little larger than the 25 ns at the SPS and LHC. The second most important parameter is the energy the electrons gained during the one bunch passing, which is

$$\langle E \rangle = \frac{e}{2m_e} \left( \frac{N_{bh} e Z_0}{2\pi b} \right)^2 \ln \left( \frac{b}{a} \right) \quad (3.1)$$

where  $Z_0 = 377 \Omega$  is the impedance in free space, and  $m_e$  is the mass of electron. Most important factor affecting  $\langle \Delta E \rangle$  is the bunch intensity.

The intensity threshold at the SPS was considerably lower than the LHC beam requirement. It was 5 to 6  $10^{10}$  at the straight sections, and 3 to 4  $\times 10^{10}$  at the dipoles. Only after several days of beam scrubbing, the LHC beam requirement was achieved.

For normal electron cloud, eRHIC have several new issues to deal with.

1. Electron multipacting in cold region. The chamber radius at the cold region is 3.46 cm, compared with 6.1 cm at warm sections. The multipacting threshold at the cold region is, therefore, lower. Once electron cloud built up, the cryogenic heat load will be of concern. Experiment data at the CERN SPS shows that the heat load is larger than 1.2 W/m under electron multipacting, which is not acceptable for RHIC cryogenic system [13].
2. Since the cold region consists 3/4 of the RHIC ring, the electron cloud induced beam instability and beam emittance will be of concern.
3. Electron cloud will present not only at the injection, but also at the ramp and storage.
4. Electron activity in dipole and quadrupole becomes relevant. The multipacting threshold at the dipoles is lower than that at the straight sections. Moreover, since the electron dose stripes in dipoles vary according to the bending field and beam intensity, the scrubbing is more difficult. As for quadrupole field, it is suspected the electrons are trapped there and stay for a long time.

The pressure rise at the cold region is probably not a problem, thanks to the cryogenic pumping.

## Plans

### RHIC pressure rise

Active study is undergoing at the RHIC in searching for the pressure rise and electron cloud remedies. Collaboration items with the eRHIC effort include,

1. Beam scrubbing, which has been demonstrated in principle, but further study is needed for incorporating it to the operation. First for proton beam, then for heavy ion beam.

2. Beam scraping study of ion desorption. The ion desorption of high energy particle at glancing angles is still a pending issue. At the RHIC Run 4, warm dipoles will be used to actually scraping ions at the wall to measure the ion desorption rate. Measurement will take place for both stainless steel and NEG pipes for comparison.
3. The relation between the beam momentum spread and the transition pressure rise remains to be clarified. By changing the RF voltage at the transition, this can be studied. The approach has a potential to provide a remedy for this pressure rise.

The RHIC effort in reducing the beam induced pressure rise is past two years has already gained much better understanding and the machine improvement. These efforts, such as baking, solenoid, beam scrubbing, beam injection pattern, and NEG coating will likely to take effect and gradually improve the RHIC performance.

### Electron cloud

The 360 bunches mode cannot be studied at the RHIC, due to the lack of beam injection apparatus. Since the situation will be very similar to the LHC, a collaboration should be pushed forward. Fortunately the intense studies have been undergoing for several years in the CERN, including numerous beam experiments at the SPS, simulation, and theoretical effort. Suggested collaboration items include,

1. Heat load problem. Experiments at the SPS, during the 2003 run, have shown that the heat load is significant enough to be treated seriously. Further data are of interest.
2. Electron activity at dipoles and quadrupoles.
3. Beam scrubbing effect at the cold region. Also in 2003 SPS experiment, it was found that the cold region scrubbing was much less effective than that at the warm region [13]. According to these results, the current LHC plan calls for initially using not higher than  $4 \times 10^{10}$  protons per bunch for 25 ns bunch spacing, and/or a 75 ns bunch spacing injection. The lengthy scrubbing scenario is under study, which is pending on several unknowns, such as the possible beam instability during the scrubbing, the maximum heat load can be tolerated, and magnet quenching problem.

The eRHIC-LHC collaboration should be on both experimental and theoretical aspects, and simulation will be an important tool.

### 180 bunch scenario

Given luminosity unchanged, it is of interest to study the benefit of using larger bunch spacing and higher bunch intensity.

Issues related with the 180 bunch (70 ns bunch spacing), with 40% increase in bunch intensity, include,

1. Electron activity will be reduced compared with the 360 bunch mode. The decrease of the electron activity is more than linearly proportional to the inverse of bunch spacing. The experimental data of the SPS are shown in Table 3.3 [14].

Table 3.3. Bunch intensity threshold versus bunch spacing from SPS experimental data.

Bunch spacing	25	50	75	ns
Bunch intensity threshold	0.3	0.6	1.2	$10^{11}$

2. In 180 bunch scenario, the total beam intensity is reduced. This will benefit at least the pressure rise in warm sections, perhaps more.
3. Heat load needs to be estimated, including the resistive wall contribution.

4. Beam scrubbing needs to be studied.

### 3.2.3 Beam Abort Issues

The general issue considered in this section is to what extent an upgrade of the present RHIC beam abort system is required to cope with the eRHIC design level beams. An eRHIC proton beam would contain  $360 \times 10^{11}$  proton bunches at an energy of 250 GeV. The specific issue which appears most likely to require some upgrade is the likelihood that beam “punch through” from a well-controlled dumping of a design level eRHIC proton beam would quench the magnet downstream of the dump absorber. In addition the increased heating and stresses in the steel section of the absorber need to be revisited.

For reference the present Accelerator Safety Envelope (ASE) limits beams in RHIC to be less than (120 proton bunches of  $2 \times 10^{11}$  particles each at 250 GeV). The ASE also sets maximum numbers for a gold beam, namely (120 gold bunches of  $2 \times 10^9$  gold ions at 100 GeV/u). The gold situation is relevant here to the extent that we try to learn from gold experience - past or future. The proton and gold ASE limits correspond to machine setups with equal magnetic fields or currents in the RHIC superconducting magnets and hence to magnets running with equal beam-heating margins before quenching. The proton and gold limits also correspond to approximately equal radiation “dose” creation outside the machine shielding for a loss of the same fraction of the entire beam. The two ASE limits do not necessarily correspond to equal risks for beam induced quenches. That the present proton ASE would be exceeded by 50% for the eRHIC design is not the subject here, but of course this dose production is a major ASE issue, which will need to be reconsidered. Also any proposed near-term beam tests toward understanding the dump absorber behavior during an eRHIC size beam dump must still cope with the RHIC ASE.

Present experience with dumping high intensity beams is given (approximately) by gold beams at 100 GeV/u and with  $60 \times 10^9$  ions and by proton beams at 100 GeV and with  $60 \times 10^{11}$  protons. The 100 GeV proton experience teaches us little since the magnets are powered with only 40% of the current required for eRHIC. The quench margin is large. The gold experience is with the right RHIC magnet currents – the right quench margin. The total beam energy is lower than eRHIC by a factor of six. As will be mentioned again below, this is not the only trouble with gaining relevant information from gold dumps.. Simulations have indicated that for gold and proton beams with equal energy the magnet heating from beam escaping the dump absorber is not equal, and unfortunately higher by a factor of 2 -3 for the proton beam.

Experience with the present abort system reliability has not been satisfactory in that the system has “prefired” too frequently. A prefire means that one out of the abort system’s five PFN–magnet modules has triggered spontaneously causing the loss of the circulating beam. The prefire starts with a very weak kick given to some of the beam and with the rise of the abort magnet currents not synchronized to the “abort gap” present in the circulating beam. A fast “retrigger” circuit greatly reduces the damage from such events (at least at past intensities) to the RHIC experiments, but has not prevented many magnet quenches (and lost beam time). The damage from prefires would scale with the intensity of circulating beam. With a factor of six more beam in the machine, losses marginally tolerable now would probably be intolerable. This situation is already not acceptable and so the problem will be solved or at least greatly improved independent of eRHIC.

The beam energy available for deposit into the dump absorber is larger than our present experience by the factor of six. As a result the heating in the absorber will increase significantly. For the RHIC design this general subject was studied and reported on by A.J.Stevens in [15]. The initial energy

deposition as the beam enters the dump absorber is predicted to be not as severe for eRHIC as for even our present running conditions with gold due to the " $Z^2$ " dependence of the initial ionization energy loss. The maximum stresses in the downstream steel section will increase, and need to be revisited. For the geometry studies in the '92 note, they were shown to be acceptable with RHIC design intensity. Stevens' work was done with an absorber design somewhat different from what was actually built several years later. In particular he is working with an upstream carbon section 1.5 meters long while the constructed absorber has 3.2 meters of carbon [16]. The longer carbon section will reduce the peak stress in the steel. Another upgrade to attack this problem is suggested in the introduction section of [17], namely to add a vertical sweeping magnet upstream of the absorber to further spread the incoming beam over the absorber face. Temperature issues with a longer time constant are also relevant. The Beam Dump section of the RHIC Design Manual states that a system to actively cool the absorber is unnecessary for beams up to four times RHIC design and bumped once per hour. The eRHIC design intensity would require revisiting this aspect of the situation.

Now the "punch through" issue is discussed. The question is: will the magnet (Q4) just downstream of the dump absorber quench if an eRHIC design intensity beam is dumped in a well-controlled way? Two RHIC reports by A.J. Stevens [18],[19] deal with this subject. The earlier report uses a less specific model for the vacuum chamber and magnet geometry. The second is fairly close to what was actually built.

Some of the conclusions from these reports are summarized here. For a geometry close to that built, and with several conservative assumptions described in the reports, there is no margin for quenching at the RHIC design proton running conditions – at 60 bunches each with  $10^{11}$  protons and at 250 GeV. This at face value implies that the eRHIC condition would push Q4 over the quenching limit by the factor of six. Also in these notes, and as mentioned above, Stevens reports that simulations suggest  $10^9$  gold ions at 100GeV/u creates a lower hot spot in the magnet coil than  $10^{11}$  protons at 250GeV by a factor of 2 to 3. Stevens simulated one possible modification from what became the as-built geometry, namely using a beam pipe for the beam circulating just beside the primary dump absorber with a 3mm wall thickness vs the "as-built" 1.25mm. This change increased the predicted quench margin by a factor between 2.5 and 5. Stevens also suggested adding a shielding "collar" at the upstream end of Q4, (the design manual speaks of adding a Q4 liner), and magnetizing the steel of the dump absorber as potentially effective modifications. He notes but does not quantify, that the amount of punch through is sensitive to the size of the abort kick – so a stronger kicker would also decrease the heating in Q4. Clearly there needs to be additional simulation work with the present geometry to see how significant a redesign is required to satisfy eRHIC, and the work by Stevens points in some reasonable directions.

Can any information be deduced from the fact that RHIC is no longer just a paper machine? Q4 has not quenched during dumps. This is a necessary condition to believe the past simulations, but not useful beyond that. Gold at 100 GeV/u and at the ASE intensity limit would be interesting, but again not sufficient since it is expected that gold is less effective in generating the quench conditions. Protons only get interesting at 250 GeV, which is not a planned running configuration for a few years. If this condition were available, then dumping at the proton ASE is certainly interesting, since that condition is only 50% away from the eRHIC design. The injector is not a limit for proton intensity, so doing such a test is not completely crazy, though obviously RHIC must be able to accelerate the beam.

### 3.2.4 Cryogenic Load Limit

RHIC is a superconducting machine and all its magnets, dipoles and quadrupoles, are superconducting magnets. Because of this most of the RHIC beam pipe is at cryogenic temperature. The limit on allowable heat load on the walls of the cold vacuum chamber provides a serious limitation on the total beam intensity which can be stored in ion rings. The capacity of the present refrigerator of the RHIC cryogenic system defines the maximum allowable heat load at the level of 0.5-1 W/m. Two dominating sources of the vacuum pipe heat load are pipe heating by the image current of the beam due to finite wall conductance and heating produced by the electron cloud.

The vacuum pipe used at the RHIC is made from stainless steel with the conductivity of  $\sigma = 2 \mu\Omega^{-1}\text{m}^{-1}$  at 4.2K. Heat load produced in the resistive walls of the vacuum pipe depends on bunch intensity  $N_b$ , number of bunches  $M$  in the beam and on the rms length  $\sigma_l$  of individual bunch. To evaluate the power  $P$  of the resistive heat load the expression derived in the paper [20] has been used:

$$P = 2I_{ave}^2 \sum_{n=1}^{\infty} R_c \left( \frac{n}{n_c} \right)^{\frac{1}{2}} \exp(-n^2 \alpha^2) \quad (3.2)$$

where  $I_{ave}$  is the average beam current,  $\alpha = M\sigma_l/R_0$  and  $R_0$  is the average ring radius. The parameters of critical resistance  $R_c$  and critical harmonic number  $n_c$  are defined by properties of the vacuum pipe such as the conductivity, mean free path length for electrons and the pipe radius. For the RHIC stainless steel vacuum pipe at 4.2K temperature these parameters are equal to:

$$R_c = 6.04 \times 10^6 \Omega, \quad n_c = \frac{8.0 \times 10^{11}}{M}$$

Due to very large value of  $n_c$  the anomalous skin effect is not important for the RHIC vacuum pipe and is not taken into account in the expression (3.2). Figure 3.21 shows results of resistive heat load calculations versus rms bunch length for different number of bunches with  $10^{11}$  proton bunch intensity. At 360 bunches the heat load limit of 0.5 W/m is reached at  $\sigma_l \approx 12\text{cm}$ . The rms bunch length value for eRHIC operation, 20cm, stays by more than factor 2 below the cryogenic limit, thus providing necessary safety margin.

Since the result of the infinite summation in the equation (3.2) is approximately proportional to  $M^{-1}\sigma_l^{-3/2}$  the resistive heat load power is proportional to  $M \cdot N_b^2$ . Then for the eRHIC luminosity in cryogenic load limit  $P_{lim}$ , at fixed bunch length, one gets dependence:  $L \sim P_{lim}/N_b$ . It shows that at the same total proton current increasing the number of particles per bunch effectively leads to lower luminosity. Increasing the number of bunches while decreasing the bunch intensity would be a way to go to higher luminosity. But it will require the serious upgrade of RHIC RF system.

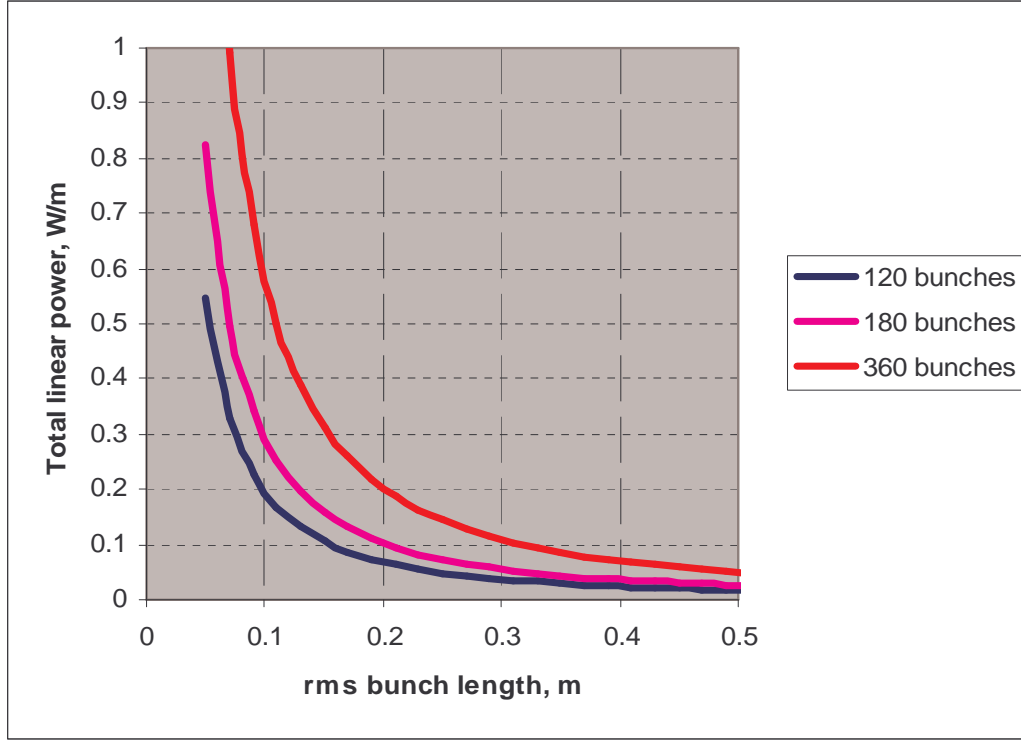


Figure 3.21: The resistive heat load power per unit length versus rms bunch length for different number of bunches with the intensity of  $10^{11}$  protons per bunch. The maximum allowable load defined by RHIC cryogenics is about 0.5 W/m.

The heat load contribution from electron cloud might be very important as demonstrated by experiments done at SPS accelerator at CERN. Heat load more than 1 W/m has been observed there at similar to RHIC bunch intensities but with smaller distance (25ns) between bunches [13]. The subject will require careful studies to evaluate a contribution from this source of heat load for eRHIC parameters.

### 3.3 Instabilities

At present we are most troubled by single bunch transverse instabilities near transition. The transverse impedance model is low by about a factor of 3 [21],[22], so we will scale the most extreme conditions from the last run to obtain threshold estimates.

For a short range transverse wake field, the rigid mode betatron tune shift is  $\Delta Q = K_0 Z I_p / A \gamma$ , where  $K_0$  is a constant that depends only on the lattice and machine impedance,  $Z$  and  $A$  are the atomic number and mass of the ion,  $I_p$  is the peak beam current, and  $\gamma$  is the Lorentz factor. When the rigid mode tune shift becomes too large, instabilities can result.

The fast head tail, or transverse mode coupling, instability threshold is reached when the rigid mode tune shift becomes comparable to the synchrotron tune. This threshold also depends on the relative length scales of the bunch and the wake field [23],[24]. For a general wakefield the dependence is fairly complicated but since the instability is due to coupling between low lying synchro-betatron modes a pessimistic estimate can be made by assuming that the wakefield is a step function. In this

case the instability threshold for a rectangular bunch is given by  $\Delta Q = Q_s / 2$ . For a 2 particle model one gets  $\Delta Q = Q_s / \pi$ , suggesting that the estimate is fairly robust.

For unstable transverse microwave modes the threshold is  $\Delta Q = K_1 |\xi + n\eta| \delta + q$ , where  $K_1$  is a constant of order unity,  $\xi$  is the un-normalized chromaticity,  $n = f / f_0$  is the ratio of the instability carrier frequency to the revolution frequency,  $\eta$  is the frequency slip factor,  $\delta$  is the fractional, rms momentum spread, and  $q$  is the rms detuning with betatron amplitude. For  $\xi = q = 0$ , and  $1/f$  equal to the bunch length, the transverse microwave threshold is similar to the fast head-tail threshold. Direct addition of the detuning and momentum dependent damping terms is a rough approximation and more accurate formulas will be considered in the future.

A high intensity study from May 30, 2003 sets strong limits on the various thresholds.

Six bunches of  $2 \times 10^{11}$  protons with  $I_p = 5.5A$  were stored with  $\gamma = 25$ . The rms bunch length was  $\sigma_t = 2.3ns$ , so  $c\sigma_t = 70cm$ . The synchrotron frequency was about  $25Hz$  and the 95% normalized transverse emittance was between 15 and 25 mm-mrad.

The rms detuning with amplitude was calculated from a model to be  $q = 2 \times 10^{-4}$ . Since the synchrotron tune was  $\approx 3 \times 10^{-4}$ , the damping from each source is comparable. For eRHIC operations the synchrotron tunes will be no smaller than those during the study. If we assume that the octupoles can always be tuned to give the same rms tune spread then thresholds during eRHIC operation can be estimated by demanding that the rigid mode tune shift be no larger than it was during this study. Take  $c\sigma_t = 15cm$ , which is the nominal bunch length during collision for eRHIC. The maximum bunch intensities calculated by this method are shown in the third column of the Table 3.4.

Table 3.4: Estimated bunch intensity thresholds for different species and energies.

gamma	Species	Threshold, same $\Delta Q$
25	Protons	4.3E10
107	Protons	1.8e11
250	Protons	4.3e11
107	Gold	5.8e9

As one can see from the Table 3.4 the low and medium energy protons are the most worrisome. However, by demanding the same tune shift we have neglected a significant benefit from the shorter eRHIC bunches. Since the eRHIC bunches are less than half as long as the bunches during the study, the synchrotron frequency in eRHIC can be more than double the value during the study without increasing the momentum spread of the bunch. Also, the octupoles were off during the study and operations with gold beams have shown that an octupole induced tune shift of comparable magnitude to the tune shift from the bare lattice can be tolerated. Therefore, it is likely that careful tuning will allow for double the intensities in the third column of the table.

With the exception of transition, single bunch longitudinal instabilities have not been observed in RHIC. These instabilities occur only when the coherent synchrotron tune shift becomes comparable to the synchrotron tune. This is equivalent to demanding that the induced voltage from the machine impedance be comparable to the rf voltage. Setting these equal gives  $|Z/n| I_p = h\omega_0^2 \sigma_t^2 V_{rf}$ , where  $|Z/n|$  is the broad band impedance,  $h$  is the rf harmonic number, and  $V_{rf}$  is the amplitude of the rf voltage. The most stringent condition occurs for protons with  $\gamma = 25$  since the proximity to transition reduces the allowed rf voltage. If we take the conservative value of  $Z/n = 3j\Omega$  and the

same momentum spread as was obtained during the study one finds a threshold intensity of  $1.8 \times 10^{11}$  protons per bunch. The actual impedance near transition is about half of the conservative estimate so no longitudinal single bunch instabilities are expected in eRHIC.

With short bunch spacing and large average current, coupled bunch instabilities are a concern. Both short and long range wakefields along with the sources and amounts of collisionless damping available are key points. Since both longitudinal and transverse single bunch instabilities are not expected the short range wakefields are not large enough to overcome the collisionless damping. Therefore, we expect coupled bunch instabilities only if the tune shifts due to long range wakefields are larger than the tune shifts due to short range wakefields. The transverse impedance due to resistive wall, abort kickers and unshielded bellows is shown in Figure 3.22: Transverse resistance (red) and reactance (blue) from the RHIC impedance model. Figure 3.22 and the resulting rigid mode coupled bunch tune shifts are shown in Figure 3.23.

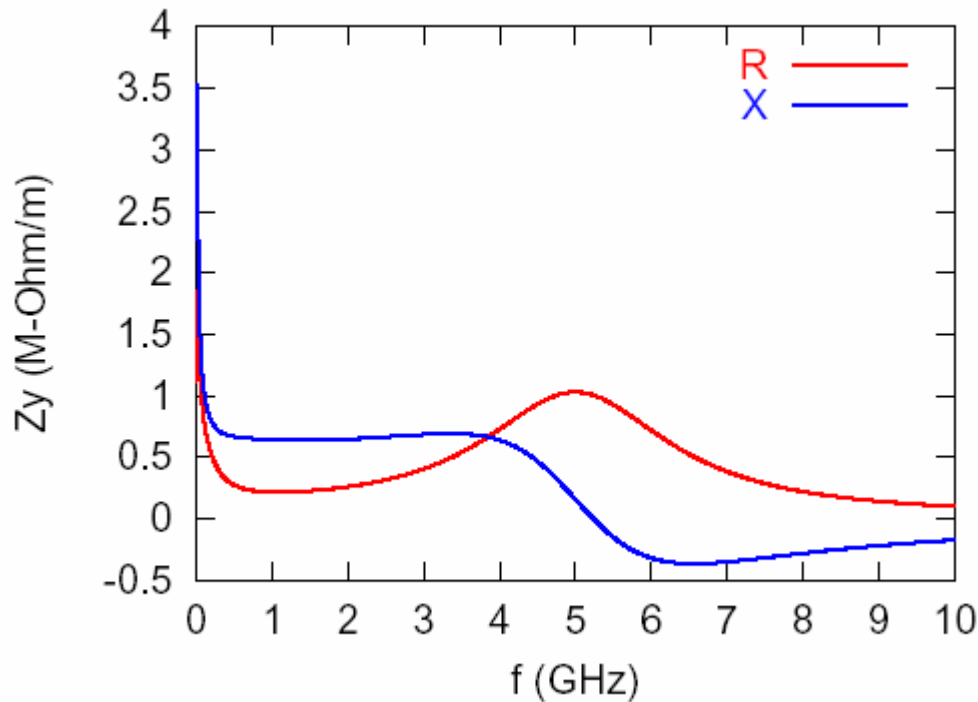


Figure 3.22: Transverse resistance (red) and reactance (blue) from the RHIC impedance model.

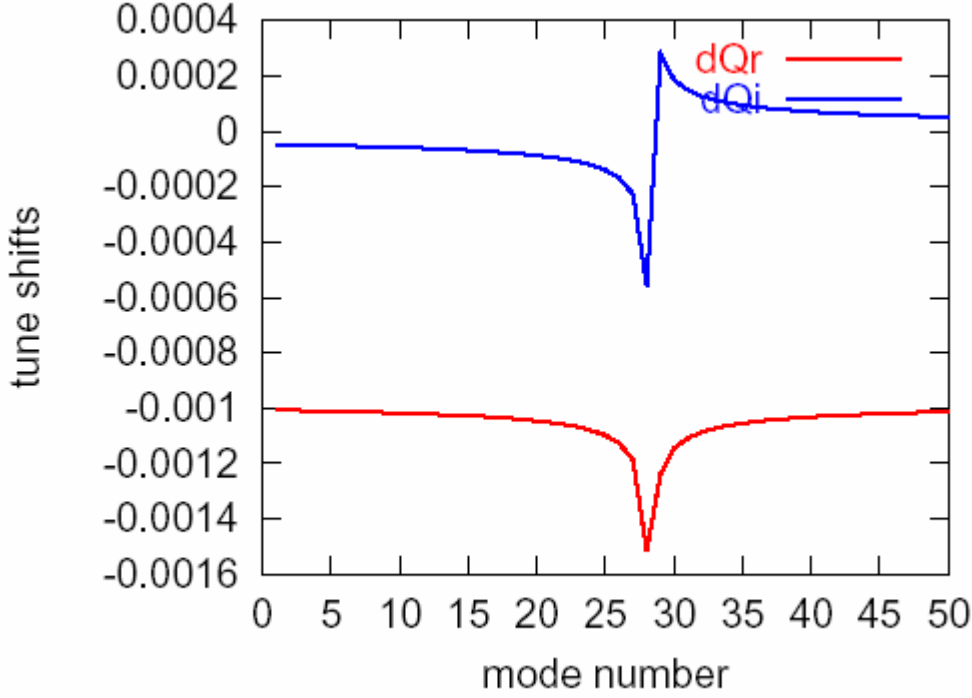


Figure 3.23: Real (red) and imaginary (blue) tune shifts for the rigid coupled bunch modes of protons with eRHIC parameters at  $\gamma = 25$ . All Landau damping is neglected.

Near the peak of the resistive wall growth rate, at mode number 29, the magnitude of the coherent tune shift is about 50% larger than the value for small mode numbers.

This is not too great a difference so if single bunch instabilities are absent we expect no problems from transverse coupled bunch modes. If there are problems then the maximum growth rate in figure 2 corresponds to an e-folding time of 5 milliseconds, which should be fairly easy to damp. Once the beams are brought into collision the nonlinear beam-beam forces will enhance the tune shift with amplitude providing even more transverse damping.

Longitudinal coupled bunch modes have not been studied in detail, but no serious problems are expected.

### 3.4 Beam Polarization Issues

#### Motion without snakes or spin rotators

To achieve a high energy polarized proton beam requires an understanding of the evolution of spin during acceleration and the tools to control it. The evolution of the spin direction of a beam of polarized protons in external magnetic fields such as exist in a circular accelerator is governed by the Thomas-BMT equation[26],

$$\frac{d\vec{P}}{dt} = -\left(\frac{e}{\gamma m}\right) \left[ G\gamma \vec{B}_\perp + (1+G) \vec{B}_\parallel \right] \times \vec{P} \quad (3.3)$$

where the polarization vector  $\vec{P}$  is expressed in the frame that moves with the particle. Here  $G = (g - 2)/2$  is the anomalous magnetic moment coefficient, and  $B_{\parallel}$  and  $B_{\perp}$  are the respective longitudinal and perpendicular components of the magnetic induction in the laboratory frame. This simple precession equation is very similar to the Lorentz force equation which governs the evolution of the orbital motion in an external magnetic field:

$$\frac{d\vec{v}}{dt} = -\left(\frac{e}{\gamma m}\right) [\vec{B}_{\perp}] \times \vec{v}, \quad (3.4)$$

where  $\vec{v}$  is the proton's velocity. From comparing these two equations it can readily be seen that, in a pure vertical field, the spin rotates  $G\gamma$  times faster than the orbital motion. Here  $G = 1.7928$  is the anomalous magnetic moment coefficient of the proton and  $\gamma$  is the Lorentz factor. In this case the factor  $G\gamma$  then gives the number of full spin precessions for every full revolution, a number which is also called the spin tune  $\nu_{sp}$ . At top RHIC energy (250 GeV) this number reaches 478. Parameters for protons as well as a few other ion species are given in Table 3.5. The Thomas-BMT equation also shows that at low energies ( $\gamma \approx 1$ ) longitudinal fields  $\vec{B}_{\parallel}$  can be quite effective in manipulating the spin motion, but at high energies transverse fields  $\vec{B}_{\perp}$  need to be used to have any effect beyond the always present vertical holding field.

Table 3.5. . Parameters for various polarized species. While deuterons and tritium ions are not presently being considered, they are included for reference. Parameters for electrons at 10 GeV are also shown for comparison.

	p	$^2\text{H}^+$	$^3\text{H}^+$	$^3\text{He}^{+2}$	$e^-$
$m$ [GeV/c <sup>2</sup> ]	0.9382720	1.8756127	2.80892823	2.8083912	0.0005109989
$G = (g - 2)/2$	1.79284734	-0.1426177	7.918194	-4.18396	0.001159652
$mc^2/G$ [MeV]	523.3418	13156.49	354.7435	-671.2216	440.6485
$R_{\text{inj}} = p_{\text{inj}}/q$ [Tm]	81.113	81.113	81.113	81.027	
$U_{\text{inj}}$ [GeV]	24.335	24.364	24.479	48.664	
$U_{\text{inj}}/n$ [GeV]	24.335	12.182	8.160	16.221	
$\gamma_{\text{inj}}$	25.9362	13.0034	8.7146	17.3280	
$G\gamma_{\text{inj}}$	46.500	-1.854	69.004	-72.500	
$R_{\text{store}} = p_{\text{store}}/q$ [Tm]	833.904	833.904	833.904	833.904	33.356
$U_{\text{store}}$ [GeV]	250.000	250.005	250.014	500.004	10
$U_{\text{store}}/n$ [GeV]	250.000	125.003	83.338	166.668	10
$\gamma_{\text{store}}$	266.4473	133.2926	89.0069	178.0394	19569.54
$G\gamma_{\text{store}}$	477.699	-19.062	704.774	-744.917	22.6938

The acceleration of polarized beams in circular accelerators is complicated by the presence of numerous depolarizing resonances. During acceleration, a depolarizing resonance is crossed whenever the spin precession frequency equals the frequency with which spin-perturbing magnetic fields are encountered. There are two main types of depolarizing resonances corresponding to the possible sources of such fields: *imperfection resonances*, which are driven by magnet errors and misalignments, and *intrinsic resonances*, driven by the focusing fields.

The resonance conditions are usually expressed in terms of the spin tune  $\nu_{sp}$ . For an ideal planar accelerator, where orbiting particles experience only the vertical guide field, the spin tune is equal to  $G\gamma$ , as stated earlier. The resonance condition for imperfection depolarizing resonances arises when  $\nu_{sp} = G\gamma = n$ , where  $n$  is an integer. Imperfection resonances for protons are therefore separated by only 523 MeV energy steps. The condition for intrinsic resonances is  $\nu_{sp} = G\gamma = kP \pm \nu_y$ , where  $k$  is an integer,  $\nu_y$  is the vertical betatron tune and  $P$  is the superperiodicity. For example at the Brookhaven AGS,  $P=12$  and  $\nu_y \approx 8.8$ . For most of the time during the acceleration cycle, the precession axis, or stable spin direction, coincides with the main vertical magnetic field. Close to a resonance, the stable spin direction is perturbed away from the vertical direction by the resonance driving fields. When a polarized beam is accelerated through an isolated resonance, the final polarization can be calculated analytically[28] and is given by

$$P_f/P_i = 2e^{-\frac{\pi|\varepsilon|^2}{2\alpha}} - 1, \quad (3.5)$$

where  $P_i$  and  $P_f$  are the polarizations before and after the resonance crossing, respectively,  $\varepsilon$  is the resonance strength obtained from the spin rotation of the driving fields, and  $\alpha$  is the change of the spin tune per radian of the orbit angle. When the beam is slowly ( $\alpha \ll |\varepsilon|^2$ ) accelerated through the resonance, the spin vector will adiabatically follow the stable spin direction resulting in spin flip. However, for a faster acceleration rate partial depolarization or partial spin flip will occur. Traditionally, the intrinsic resonances are overcome by using a betatron tune jump, which effectively makes  $\alpha$  large, and the imperfection resonances are overcome with the harmonic corrections of the vertical orbit to reduce the resonance strength  $\varepsilon$  [29]. At high energy, these traditional methods become difficult and tedious.

### Effect of Siberian snakes

By introducing a ‘Siberian snake’ [30], which generates a  $180^\circ$  spin rotation about an axis in the horizontal plane, the stable spin direction remains unperturbed at all times as long as the spin rotation from the Siberian snake is much larger than the spin rotation due to the resonance driving fields. Therefore the beam polarization is preserved during acceleration. An alternative way to describe the effect of the Siberian snake comes from the observation that the spin tune with the snake is a half-integer and energy independent. Therefore, neither imperfection nor intrinsic resonance conditions can ever be met as long as the betatron tune is different from a half-integer.

Such a spin rotator is traditionally constructed by using either solenoidal magnets or a sequence of interleaved horizontal and vertical dipole magnets producing only a local orbit distortion. Since the orbit distortion is inversely proportional to the momentum of the particle, such a dipole snake is particularly effective for high-energy accelerators, e.g. energies above about 30 GeV. For lower-energy synchrotrons, such as the Brookhaven AGS with weaker depolarizing resonances, a partial

snake[31], which rotates the spin by less than  $180^\circ$ , is sufficient to keep the stable spin direction unperturbed at the imperfection resonances.

### Acceleration of polarized protons

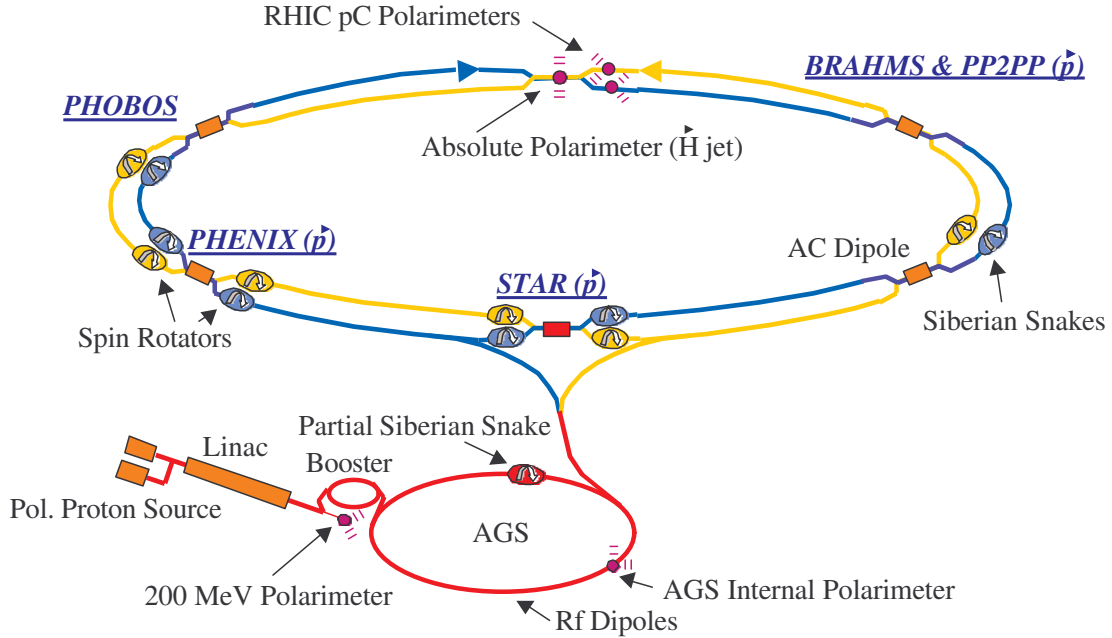


Figure 3.24. Present layout of RHIC accelerator complex for polarized protons.

Each snake and rotator is composed of four helical dipole magnets[32]. Helical field magnets have some distinctive advantages over more conventional transverse snakes or rotators: (i) the maximum orbit excursion is smaller, (ii) the orbit excursion is independent of the separation between adjacent magnets, and (iii) they allow an easier control of the spin rotation and the orientation of the spin precession axis.

In an ideal helical dipole magnet to be used for our purposes, the central dipole field should rotate through a complete  $360^\circ$  from one end of the magnet to the other. In a real magnet, of course, the fields at the ends of the magnet will also contribute to the particle dynamics. We require that the

integrals  $\int B_x d\ell$  and  $\int B_y d\ell$  are both less than  $0.05 \text{ Tm}$ . The maximum body field will thus rotate through an angle less than  $360^\circ$  along the axis of the magnet. Moreover, in order to simplify the construction of the snakes/rotators, a solution has been found with all magnetic modules identical in both devices. For the snakes each helix is right handed with the field at the end being vertical. For the rotators, the helices alternate between right and left handedness with the field at the end of each helix being horizontal.

The orbit though an ideal helix will have the incoming and outgoing rays parallel but transversely displaced. In order to have a net displacement of zero through a snake we require that the offset be canceled by powering in pairs with opposite fields. The inner pair are wired in series with opposite polarity and powered by a common power supply. The outer pair are also wired in series with opposite polarity to a second supply. Figure 3.25 shows the field components, design orbit, and spin

rotation through a snake at injection energy. At 250 GeV the required fields are almost the same, but the orbit displacement in the middle of the snake is only about 3 mm.

By operating the helices at different currents it is possible to adjust both the amount of spin rotation (angle  $\mu$ ) and axis of rotation. With the helices wired as described above, the axis of rotation for the snake is in the horizontal plane at an angle  $\phi$  from the longitudinal direction. Figure 3.26 shows the dependence of  $\mu$  and  $\phi$  on the two field settings –  $B_1$  for the outer pair of helices, and  $B_2$  for the inner pair.

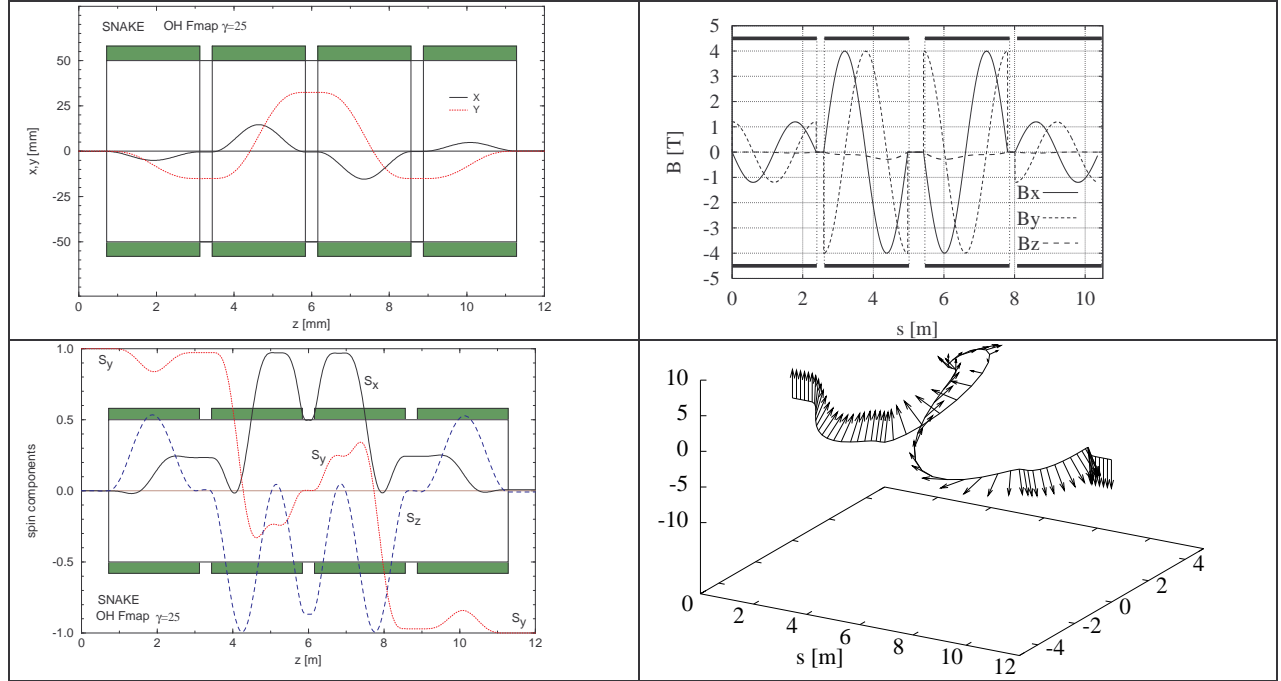


Figure 3.25: Field, orbit, and spin tracking through the four helical magnets of a Siberian snake at  $\gamma = 25$ . The spin tracking shows the reversal of the vertical polarization.

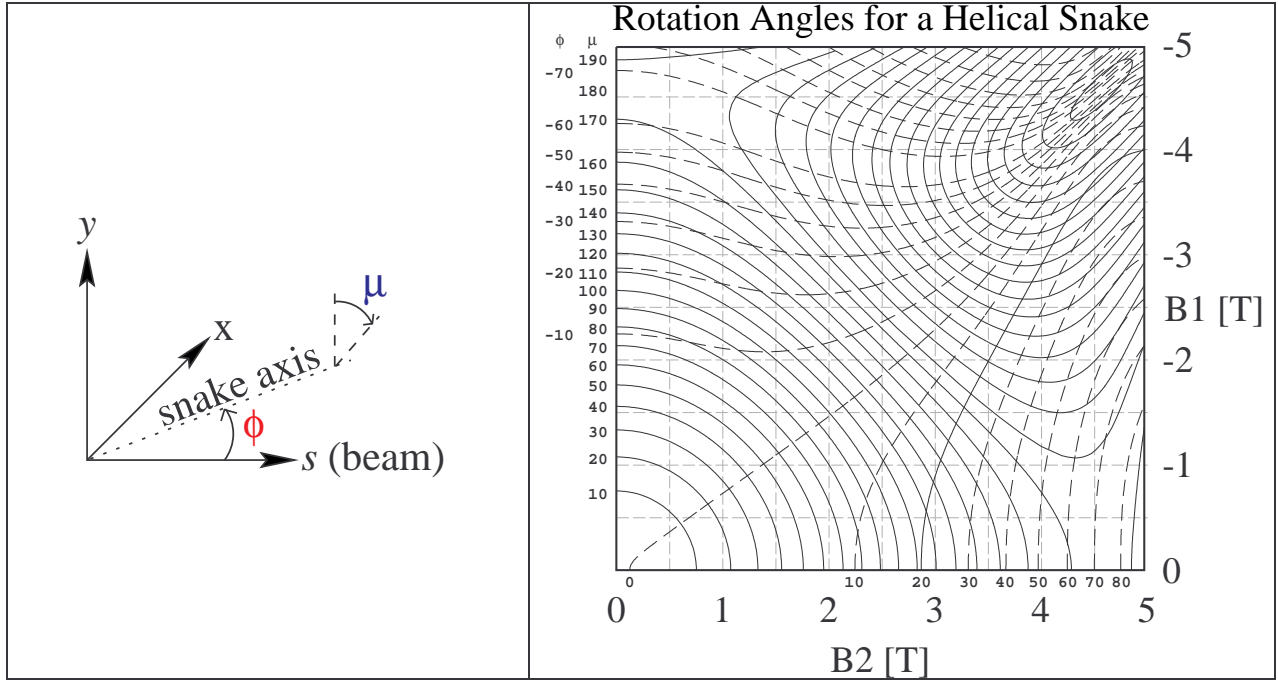


Figure 3.26: Change of the direction of the snake rotation axis as a function of magnet excitation. This calculation uses a simplified analytical expression for the snake magnetic field. The rotation axis of the snake is  $\phi$  (dashed), and  $\mu$  (solid) is the rotation angle.  $B_1$  is the field strength of the outer pair of helices, and  $B_2$  is the field strength of the inner pair.

For the ion beam in the electron-ion interaction region, a pair of spin rotators identical to the existing rotators around STAR and PHENIX may be used. Spin rotator parameters are listed in Table 3.6. The result of the orbit and spin tracking is shown in Figure 3.27. At STAR and PHENIX, the direction of the spin rotator beam line is at a horizontal angle  $\theta = 3.674$  mrad with the direction of the adjacent insertion, the spin should emerge from the rotator in the horizontal plane and at an angle  $G\gamma\theta$  with the rotator axis in order to obtain a longitudinal polarization through the insertion region. The needed rotation is therefore dependent on the beam energy. The values of the field needed to provide a longitudinal polarization at different energies are shown in Figure 3.28. The rotators will be turned on only after accelerating the beam to the desired storage energy.

In the electron-ion interaction region, the incoming and outgoing rotators are parallel to the beam at the interaction point. In this case, there is no net precession between the rotators and the collision point, so to obtain longitudinal polarization the rotators will be set with fields corresponding to the intersection of the  $\theta = 0^\circ$  and  $\mu = 90^\circ$  contours of Figure 3.28. With no extra precession from beam splitter magnets, there is no need to change values for different energies.

Table 3.6. Parameters for the spin rotator magnets. Helical magnets alternate right-handed and left-handed, and all begin and end with horizontal fields. The central field strengths were optimized to include end effects of the magnets, and are calculated for longitudinal polarization at the beam collision point.

Number of helical magnets				4	
Total length				10.56 m	
Magnet bore				100 mm	
Helical Magnets					
	Length (effective)	Field helicity	Field orientation at entrance/exit	Field (25 GeV)	Field (250 GeV)
1	2.40 m	right-handed	Horizontal	2.1 T	3.5 T
2	2.40 m	left-handed	Horizontal	2.8 T	3.1 T
3	2.40 m	right-handed	Horizontal	2.8 T	3.1 T
4	2.40 m	left-handed	Horizontal	2.1 T	3.5 T
Max. orbit excursion (hor./ver.) (25 GeV)				25 mm / 10 mm	
Total field integral				23 T-m	
Orbit lengthening (25 GeV)				1.4 mm	

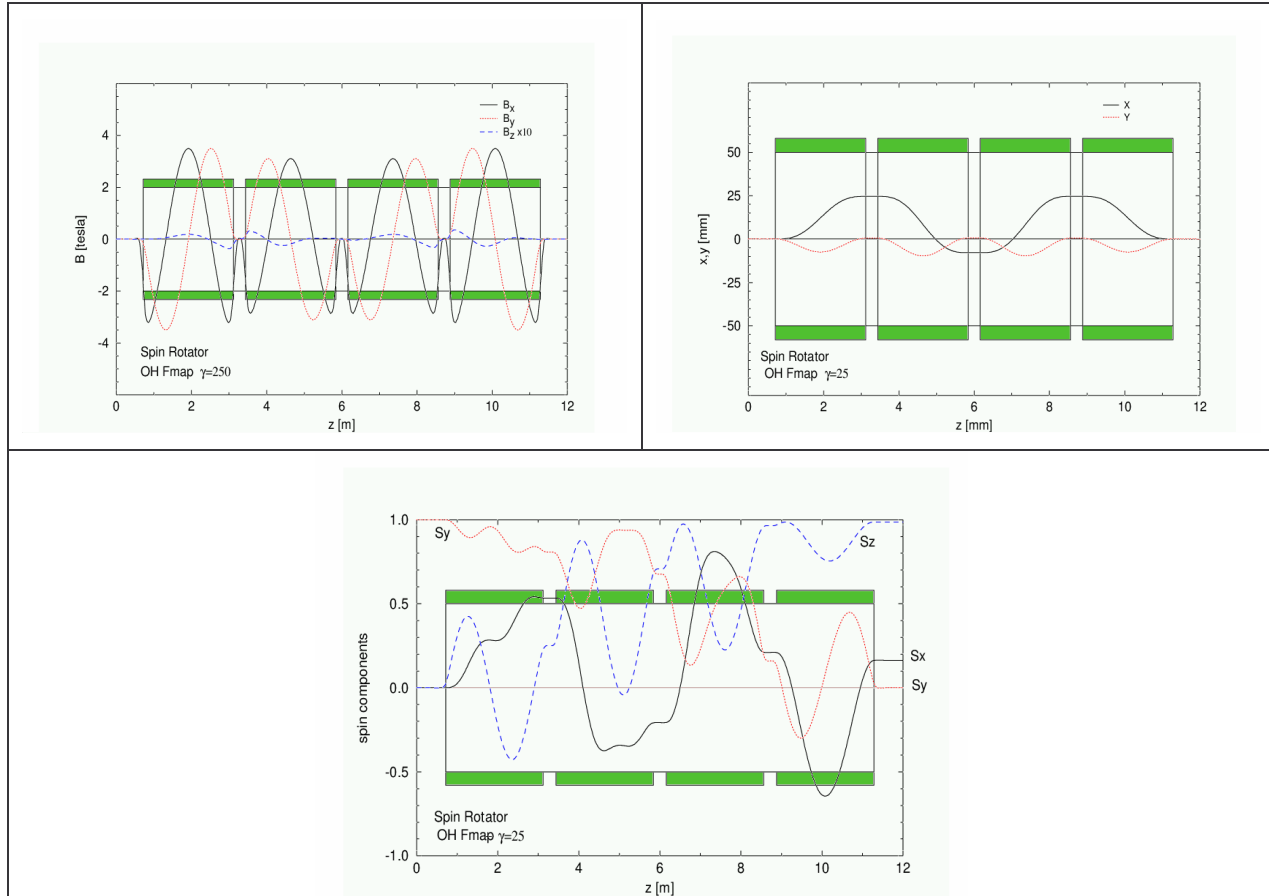


Figure 3.27: Field, orbit, and spin tracking through the four helical magnets of a spin rotator at  $\gamma = 25$ . In this example, the spin tracking shows how the polarization is brought from vertical to horizontal.

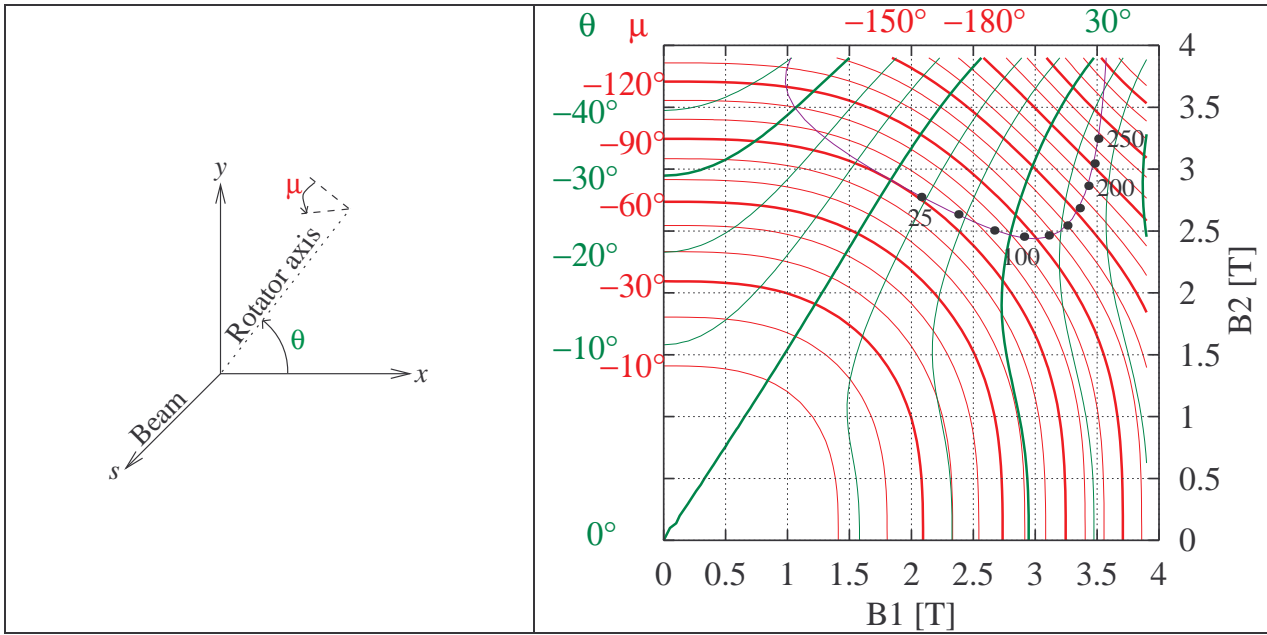


Figure 3.28: Excitation of the two pairs of helical magnets in the rotator to achieve longitudinal polarization in the insertion of RHIC, for various beam energies. The large dots indicate settings for the rotators around the STAR and PHENIX detector. For the eRHIC collision point, there is no net rotation between the collision point and the adjacent rotators, so the desired setting for longitudinal polarization corresponds to  $\theta = 0^\circ$  and  $\mu = 90^\circ$ .

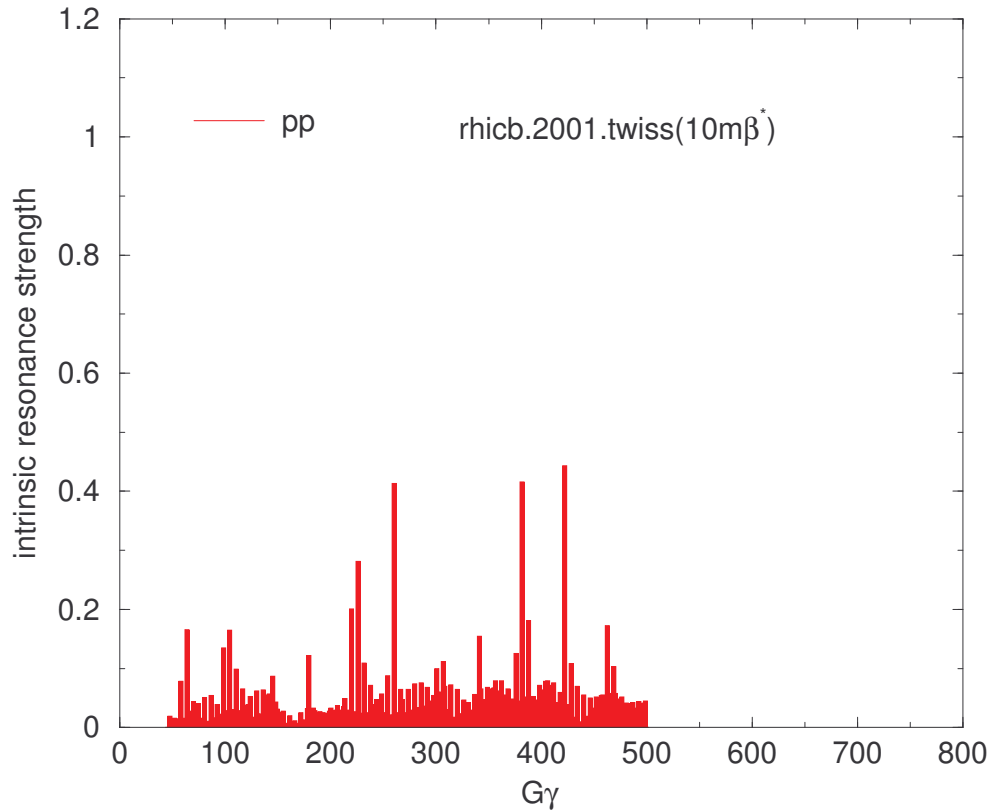


Figure 3.29: DEPOL calculation of intrinsic resonance strengths for polarized protons in RHIC without snakes.

### Acceleration of polarized ${}^3\text{He}^{+2}$ ions

In order to scale to a different ion species such as  ${}^3\text{He}^{+2}$ , we should examine the parameters for a single RHIC rotator helix. The pitch is given by

$$k = \frac{2\pi}{\lambda}, \quad (3.6)$$

where  $\lambda = 2.41\text{m}$  is positive for a right-handed and negative for a left-handed helix. The rotation axis is given by

$$\hat{n} = \frac{k\hat{z} + \kappa\hat{x}}{\sqrt{\kappa^2 + k^2}} \quad (3.7)$$

where

$$\kappa = \frac{q}{p}(1 + G\gamma)B \quad (3.8)$$

with a precession angle of

$$\alpha = 2\pi \left[ \sqrt{1 + \left(\frac{\kappa}{k}\right)^2} - 1 \right]. \quad (3.9)$$

The transverse step of the trajectory is

$$\Delta x = \frac{q}{p} \frac{B\lambda}{k} = \frac{q}{p} \frac{\lambda^2}{2\pi} B. \quad (3.10)$$

The Lorentz factor for a given rigidity is

$$\gamma = \sqrt{1 + \left(\frac{ZeR}{mc}\right)^2}, \quad (3.11)$$

for an ion with with rigidity  $R = p/q$ , charge  $Ze$  and mass  $m$ . We want to have the same spin precession in snakes and rotators for other ions as for protons. Keeping the rigidity constant for different ion species, we should scale the fields as

$$B_i = \frac{1 + G_p \sqrt{1 + \left(\frac{eR}{m_p c}\right)^2}}{1 + G_i \sqrt{1 + \left(\frac{eR}{m_i c}\right)^2}} B_p \quad (3.12)$$

from protons to ions, where the  $i$ -subscript indicates parameters for the ion.

Assuming that the maximum energy at storage corresponds to a rigidity of  $R = 834\text{Tm}$ , then the maximum value of Lorentz factor for  ${}^3\text{He}^{+2}$  would be 178.039. Values for injection and storage energy are given in Table 3.5. It should be noted that there are about 56% more precessions for  ${}^3\text{He}^{+2}$  than protons at the same rigidity. Since the precessions for  ${}^3\text{He}^{+2}$  are larger, we should expect more depolarizing resonances. The resonances will also be stronger. This can be seen by comparing DEPOL calculations with no snakes for protons in Figure 3.29 and  ${}^3\text{He}^{+2}$  in Figure 3.30. In principle with snakes, acceleration of  ${}^3\text{He}^{+2}$  should be possible to full energy, but the closed orbit and tune requirements will be more severe for  ${}^3\text{He}^{+2}$ . The scaling to  ${}^3\text{He}^{+2}$  for the rotators actually lowers the required fields to obtain longitudinal polarization. Table 3.7 gives rough values of field settings for the snakes and rotator settings (electron-ion experiment). Since the transverse excursions in scale

with field (See Eq.(3.10) ), the beam excursions for  ${}^3\text{He}^{+2}$  in snakes and rotators will be about 65% of the size of those for protons at the same rigidity.

Table 3.7. Approximate field settings for snakes (outer:  $B_{1,s}$ , inner:  $B_{2,s}$ ) and rotators (outer:  $B_{1,r}$ , inner:  $B_{2,r}$ ) at full energy. Note that even though  $G$  has opposite signs for protons and  ${}^3\text{He}^{+2}$ , the snakes power supplies do not need to be reversed, since we only require that the snake axes be at  $90^\circ$  to each other. Similarly the rotator supplies at the electron-ion experiment do not need to be reversed, since the precession is about the radial  $\hat{x}$ -axis in the rotators.

	p	${}^3\text{He}^{+2}$
$B_{1,s}$ [T]	1.2	0.77
$B_{2,s}$ [T]	4.0	2.57
$B_{1,r}$ [T]	1.8	1.16
$B_{2,r}$ [T]	2.9	1.87

### Other possible species

Acceleration of tritium ions would probably be similar to  ${}^3\text{He}^{+2}$ . Deuterons have a considerably smaller anomalous magnetic moment coefficient which would require much higher field magnets for full snakes. It might be possible to deal with deuterons by operating a single snake as a partial snake. Scaling a 100% snake for protons to deuterium makes about an 8% snake. With only a single snake, the snake axis could be in any direction, so we might consider ramping the snake to a higher strength up the ramp. Strong intrinsic resonances might be handled by an ac dipole as we have done in the past with polarized protons in the AGS.

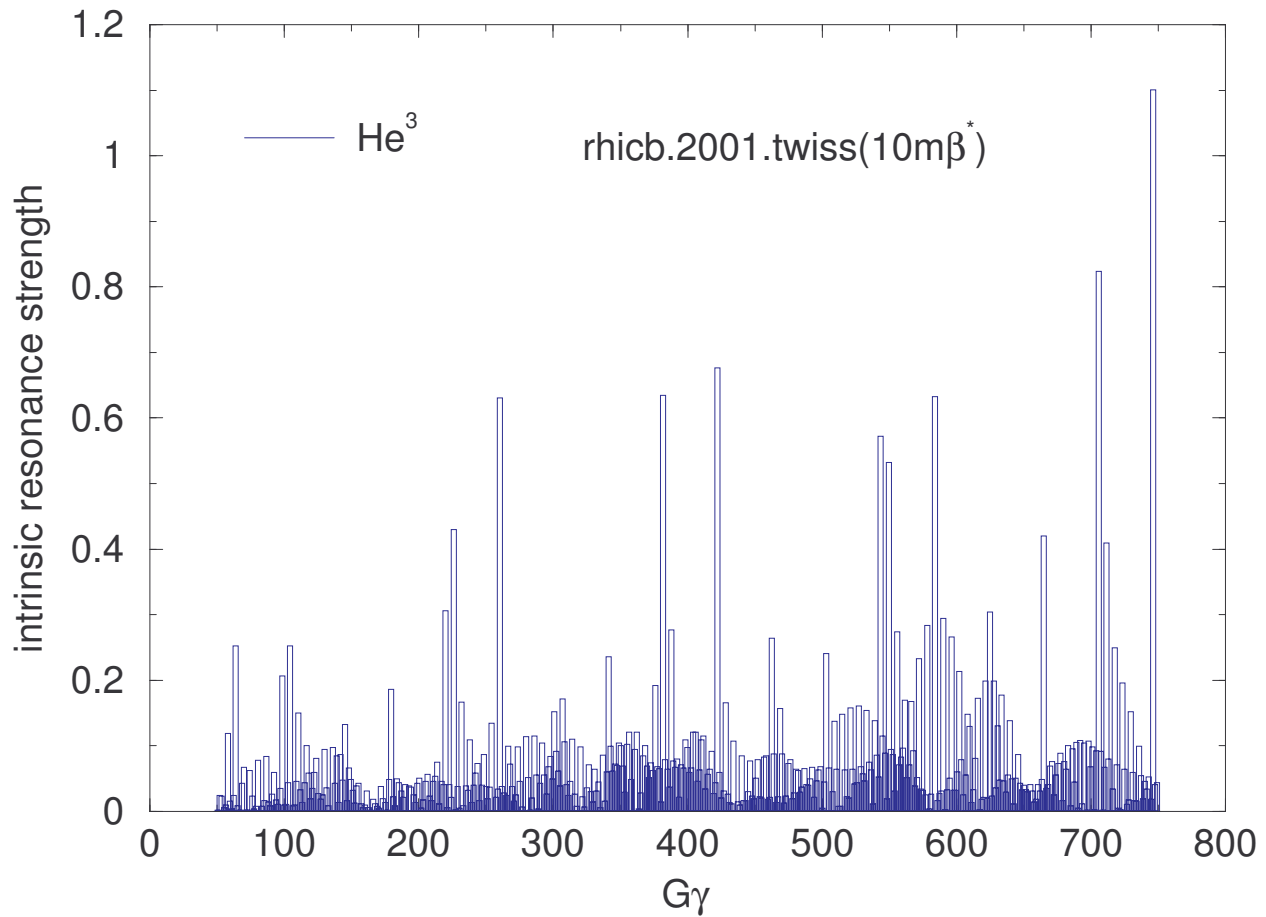


Figure 3.30: DEPOL calculation of intrinsic resonance strengths for polarized  $\text{He}^3$  ions in RHIC without snakes. Compare this with Figure 3.29. Here there are more resonances, and they are stronger than for protons.

## References:

1. V.V. Parkhomchuk and I. Ben-Zvi, Electron Cooling for RHIC, Design Report 2001.
2. I. Ben-Zvi et al., R&D towards cooling of RHIC collider, COOL'03, May 2003, Japan.
3. D. Wang et al., Proc. PAC'03, Portland, Oregon. USA 2003.
4. J. Kewisch et al., Proc. PAC'03, Portland, Oregon. USA 2003.
5. W.W. Zhang et al., PRST-AB **3**, 122401 (2000).
6. D.L. Bruhwiler et al., Proc. PAC'03, Portland, Oregon USA 2003.
7. Code SimCool was originally written in BINP (Russia) and is now being developed at BNL.
8. I.N. Meshkov et al., Proc. Beam Cooling and Related Topics, Bad Honnef, Germany, 2001.
9. Ya. Derbenev, Proceedings of EPAC'00 (Vienna, Austria), p.8, 2000.
10. K.Y. Ng, PRSTAB 061002 (2002)
11. S.Y. Zhang et al, PAC, 2003, Portland, Oregon.
12. J.M. Jimenez, Pressure rise workshop. Dec. 2003, BNL.
13. F. Ruggiero, Pressure rise workshop. Dec. 2003, BNL.
14. G. Arduini, Chamonix XIII, Jan. 2004

15. A.J.Stevens ,“Maximum Energy Deposition Densities in the Internal Dump”, AD/RHIC/RD-41, June, 1992.
16. Beam Absorber section of the RHIC Design Manual.
17. The Beam Dump System in the RHIC Design Manual.
18. A.J.Stevens, “Preliminary Study of Energy Deposition Downstream of the Internal Dump”, AD/RHIC/RD-33, January, 1992.
19. A.J.Stevens, Energy Deposition Downstream of the Internal Dump”, AD/RHIC/RD-97, December, 1995.
20. A.Ruggiero, S.Peggs, RHIC/AP/46, November 1994.
21. S.Y. Zhang, et all, EPAC02, Paris, p.1112, 2002.
22. M. Blaskiewicz, et all, PAC03, Portland, p.3026, 2003.
23. B.Zotter CERN/ISR-TH/82-10, 1982.
24. M. Blaskiewicz prstab 1, 044201, 1998.
25. “RHIC Design Manual”, Brookhaven National Laboratory; *Nucl. Inst. and Meth.*, **A499** (2003).
26. L.H. Thomas, Phil. Mag. , 1 (1927); J. Frenkel, Z. Phys. , 243 (1926); V. Bargmann, L. Michel, V.L. Telegdi, Phys. Rev. Lett. , 435 (1959).
27. I. Alekseev et al., “Polarized proton collider at RHIC”, *Nucl. Inst. and Meth.*, **A499** 392 (2003); I. Alekseev et al., *Design Manual Polarized Proton Collider at RHIC*, Brookhaven National Laboratory (1998).
28. M. Froissart and R. Stora, Nucl. Instr. Meth., , 297 (1960).
29. T. Khoe et al., Part. Accel. , 213 (1975); J.L. Laclare et al., J. Phys. (Paris), Colloq. , C2-499 (1985); H. Sato et al., Nucl. Inst. Meth., Phys. Res. Sec A, 617 (1988); F.Z. Khiari, et al., Phys. Rev. D, 45 (1989).
30. Ya.S. Derbenev et al., Part. Accel. , 115 (1978).
31. T. Roser, AIP Conf. Proc. No. 187, ed. K.J. Heller p.1442 (AIP, New York, 1988).
32. V.I.Ptitsin and Yu.M.Shatunov, Helical Spin Rotators and Snakes, Proc. Third Workshop on Siberian Snakes and Spin Rotators (A.Luccio and Th.Roser Eds.) Upton, NY, Sept. 12-13,1994, Brookhaven National Laboratory Report BNL-52453, p.15.
33. A.U.Luccio, Program SNIG, unpublished, and SNIG Formalism Proc. Third Workshop on Siberian Snakes, loc. cit., p. 193. Also: “Numerical Optimization of Siberian Snakes and Spin Rotators for RHIC”, Proc. Adriatico Conf. Trieste, Italy, Dec. 1995, World Scientific, and: Spin Note AGS/RHIC/SN008.
34. A.U.Luccio, “Optimization of Spin Angles from a Helix Field Map”, Spin Note AGS/RHIC/SN042, Upton, Nov.5, 1996.
35. E.D.Courant, “Possibilities of Accelerating Polarized D,  $^3\text{He}$  and other ions in RHIC”, AGS/RHIC/SN No. 066 (1997).
36. W.W. MacKay, et al., Superconducting Helical Snake Magnets: Design and Construction, p.163, DESY-PROC-1999-03.